

Investigating The Use Of Quadrupolar Nuclei for NMR-Based Quantum Information Processing

A thesis submitted in partial fulfillment of the requirement
for the degree of Bachelor of Science in Physics from
The College of William and Mary

by

Timothy W. Milbourne

Accepted for Honors
(Honors or no-Honors)

Gina L. Hoatson
Dr. Gina K. Hoatson, Advisor

H. Krakauer
Henry Krakauer, Physics

R. L. Vold
Dr. Robert L. Vold, Applied Science

T. K. Meldrum
Dr. Tyler K. Meldrum

Williamsburg, VA
April 23, 2014

ABSTRACT

In this thesis, we apply quantum logic gates to a two-qubit register using the techniques of nuclear magnetic resonance (NMR spectroscopy). We create a lyotropic solution of sodium decyl sulfate (SDS), deuterium oxide (D_2O), and decanol in the nematic phase, which functions as our quantum register. Using sequences of single-quantum selective pulses, we generate pseudopure initial states. Using SR, a MatLab-based spin response simulator, we check that the pulse sequences produce the appropriate pseudopure states. We then apply a CNOT quantum logic gate to each initial state. Each pseudopure state reacts as expected to the CNOT gate: while some extra excitations occur, they are generally small compared to the rest of the spectrum. These extra excitations may be the result of imperfect phase cycling in our pseudopure pulse sequences, which would leave non-zero coherences between states. These coherences could interfere with the resulting NMR spectra, producing the additional observed excitations.

1. Introduction

In this project, I am attempting to implement quantum computing algorithms using the techniques of nuclear magnetic resonance (NMR) spectroscopy. In particular, we use the energy levels of a spin- $3/2$ sodium nuclei as a two qubit register for rudimentary quantum algorithms.

At the most basic level, a quantum computer is any device which stores information within a quantum system. In a classical computer, information is stored in binary bits, which take values of 0 or 1. At the quantum level, an analogous system can be constructed with two level quantum bits (typically called “qubits”), whose quantum states correspond to the 0 and 1 state of the classical bit. Unlike their classical counterparts, these qubits may also occupy any normalizable superposition of the two states. As a result, a quantum computer would be able to perform a large number of parallel calculations, allowing them to quickly execute programs which would be unable to run efficiently on a conventional computer. Calculating the prime factors of large numbers, for instance, is incredibly time-consuming for a conventional computer. A quantum computer in contrast, can perform the same calculation in a much shorter time frame using Shor’s algorithm or some other quantum factorization algorithm.

In order to serve as a physically-realizable quantum computer, any proposed quantum processor must satisfy five requirements known as the DiVincenzo criteria. (1) A usable quantum computer must consist of a scalable physical system with well characterized qubits, (2) it must be easily set to an initial state, (3) it must use a set of universal gates, (4) there must be some method of measuring specific qubits,

and (5) the qubit's decoherence time must be longer than the average gate operation time [1]. Although typically associated with material science or molecular biology research applications, the techniques of nuclear magnetic resonance (NMR) spectroscopy satisfy these criteria. In this method of quantum information processing (QIP), nuclear spins are used as qubits. These spins are well isolated from their environment, and therefore satisfy the first DiVincenzo criterion. Sequences of standard NMR pulses can then be used to coherently manipulate the state of these spins, satisfying the second, third, and fourth parts of the criteria. The generally long relaxation times (in comparison with the length of a typical pulse sequence) of atomic nuclei ensure that NMR QIP satisfies the last criterion as well. In our experiments, we use pulse lengths between 0.3 – 0.5 *ms*. The spin-spin relaxation time (T_2) of the system, in contrast, is around 500 *ms*. The field of NMR QIP has advanced at a rapid rate: as of 2012, NMR-based quantum processors of up to thirteen qubits have been experimentally realized [1].

In this project, we successfully produced a lyotropic liquid crystal solution of sodium decyl sulfate (SDS), deuterium oxide, and decanol. After much experimentation, this sample was successfully manufactured and characterized. We then developed an optimal method of packing the sample for use in NMR experiments, and then optimized the set of radiofrequency pulses necessary for implementing our quantum algorithms. These pulses were then used to generate pseudo-pure initial states for our processor (as per the second DiVincenzo criterion). Finally, we were able to implement a basic quantum logic gate, the controlled NOT (CNOT) gate. This thesis begins with a description of the basic theory underlying the project. In particular, I provide a physical and mathematical overview of NMR spectroscopy, and a basic look at the nuclear interactions underlying our system. I then provide a more in-depth discussion of quantum computing, and how NMR may be used as a quantum computing platform. With a theoretical foundation in place, I then discuss the experimental progress outlined above, as well as our current results and hopes for future progress.

This project represents the NMR laboratory's first foray into the world of quantum information processing, and will hopefully serve as a foundation for future work in this field. In particular, the basic CNOT logic gates implemented in this project may be strung together into larger quantum algorithms,

allowing us to perform basic quantum calculations. Additionally, the results of this project may be generalized to higher spin nuclei, which would serve as a larger quantum register and would allow for the development of more complex algorithms. In particular, we hope to extend our work to spin- $7/2$ nuclei, such as cesium or scandium, which will act as a three qubit register.

2. Theory

2.1 Principles of Nuclear Magnetic Resonance (NMR) spectroscopy

NMR spectroscopy makes use of radiofrequency pulses to manipulate the quantum mechanical state of a spin system. In this process, nuclei with spin I are placed in a static magnetic field B_0 , which we take to be pointing in along the z -axis ($\vec{B}_0 = B_0\hat{z}$). The Zeeman Hamiltonian for the nuclei is then given by

$$\hat{H} = -\vec{\mu}_0 \cdot \vec{B}_0 = -\gamma\hbar\hat{I} \cdot \vec{B}_0 = -\gamma\hbar\hat{I}_z B_0 \quad (1)$$

Here $\vec{\mu}_0 = \gamma\hat{I}$ is the magnetic moment of the nucleus, γ is a nucleus-specific parameter known as the gyromagnetic constant, and \hat{I} is the vector operator for nuclear spin angular momentum. Solving the Schrödinger equation for this system, we find energies of

$$E_{m_l} = \gamma(m_l\hbar)B_0 = m_l\omega_0\hbar \quad (2)$$

where $\omega_0 = \gamma B_0$ is the nucleus-specific Larmor frequency. We therefore find that a particle of spin-3/2 has its energies split into three evenly spaced levels, corresponding to $m_l = 3/2, 1/2, -1/2,$ and $-3/2$. (See Fig. 1.)

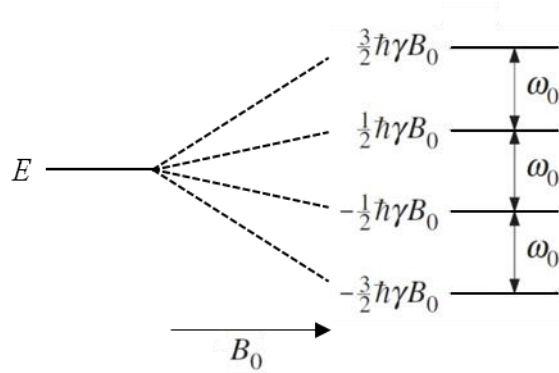


Figure 1: Splitting of energy level E into four energy levels, E_{m_l} by the Zeeman interaction. The energy levels are evenly spaced, with $\Delta E = \omega_0\hbar$.

By applying radiofrequency (r.f.) pulses centered on the Larmor frequency, we can excite specific energy transitions among Zeeman spin states. These r.f. pulses rotate the net magnetization vector, which

then precesses about the applied field at the Larmor frequency. The precessing magnetization vector induces a voltage in the pickup coil of an NMR probe. Plotting this time-dependent voltage gives a free induction decay (FID). Taking the Fourier transform of the FID produces a spectrum of the given nuclei's resonant frequencies. In material science and biological research, the resulting frequency distribution can be used to ascertain electronic structural properties of the material in question.

2.2 Quadrupolar Nuclei

Nuclei with spin $I > 1/2$ have asymmetrical electric charge distributions. As a result, these nuclei undergo interactions with local electric field gradients, known as quadrupolar coupling. To first order, the Hamiltonian for the quadrupolar interaction between a spin- I nucleus and an axially symmetric electric field gradient, q_{zz} is given by

$$\hat{H}_Q = \frac{e^2 Q q_{zz}}{4I(2I-1)} (3\hat{I}_Z^2 - \hat{I}^2) \quad (3)$$

where the product $e q_{zz}$ describes the electric field gradient, and Q give the quadrupolar moment of the nucleus. The electric field gradient is taken to be in the z direction. The form of the Hamiltonian may be simplified by defining ω_Q , the quadrupolar frequency, as follows [2], [3]:

$$\omega_Q = \frac{3e^2 Q q_{zz}}{2I(2I-1)} \quad (4)$$

Rewriting the interaction Hamiltonian in terms of this interaction frequency, we find that

$$\hat{H}_Q = \hbar \frac{\omega_Q}{6} (3\hat{I}_Z^2 - \hat{I}^2) \quad (5)$$

Using perturbation theory, we may now find the energy perturbations due to the quadrupolar interaction.

These are given by:

$$E_{m_l, q} = \frac{1}{6} \omega_Q \hbar (3m_l^2 - I(I+1)) \quad (6)$$

Now, let us consider a quadrupolar nucleus placed in an external magnetic field. In a nematic liquid crystal, asymmetric molecules align along a preferred direction. For the long SDS chains in our system, the field gradient q_{zz} lies along the preferred direction of the nematic phase. Consider the case

where the applied magnetic field lies along the z axis, and the field gradient is along a z' , which makes an angle θ with the z axis. The Zeeman energies and quadrupolar perturbations for each value of m_l are given in Table 1:

Table 1: Energy Perturbations Of The Hamiltonian

m_l	Zeeman Energy	Quadrupolar Perturbation
3/2	$\frac{3}{2}\omega_0\hbar$	$\frac{1}{2}\omega_Q\hbar$
1/2	$\frac{1}{2}\omega_0\hbar$	$-\frac{1}{2}\omega_Q\hbar$
-1/2	$-\frac{1}{2}\omega_0\hbar$	$-\frac{1}{2}\omega_Q\hbar$
-3/2	$-\frac{3}{2}\omega_0\hbar$	$\frac{1}{2}\omega_Q\hbar$

We can show that the energies of this system are given by $E_{m_l} = m_l\omega_0\hbar + A(\theta)E_{m_l,q}$, where $A(\theta) = \frac{1}{2}(3\cos^2\theta - 1)$. Notice that the quadrupolar interaction produces unevenly spaced energy levels: when $\theta = 0$, the $3/2 \rightarrow 1/2$ levels are separated by $(\omega_0 + \omega_Q)\hbar$, the $1/2 \rightarrow -1/2$ levels are separated by $\omega_0\hbar$, and the $-1/2 \rightarrow -3/2$ levels are separated by $(\omega_0 - \omega_Q)\hbar$. (See Fig. 2.) As a result, the transitions between them can be independently excited and measured using frequency-selective NMR pulses. In the language of quantum computing, the first order energy perturbation allows our quantum algorithms to change the state of individual qubits.

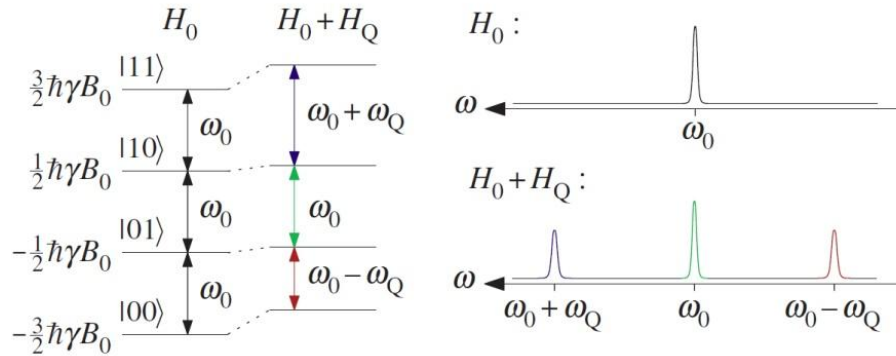


Figure 2: Energy levels and corresponding NMR spectra for a spin-3/2 nuclei. The figure includes the unperturbed Zeeman energy levels (H_0) and first perturbations due to the quadrupolar interaction, ($H_0 + H_Q$) [1].

2.3 The Density Matrix

While the description of NMR spectroscopy given in Section 2.1 examines the effect of radiofrequency pulses on individual spins, NMR experiments typically involve samples with many ($\sim 10^{18}$) spins. It is obviously impractical to calculate macroscopic properties, such as the effects of applied pulses on the sample by considering every spin individually. Instead, we may take a statistical approach to the problem by taking an ensemble average. (Note that this derivation of the density matrix follows Levitt's presentation in [4].)

Consider a single spin, whose most general wavefunction is a linear superposition of eigenstates, ϕ_i , with coefficients c_i :

$$|\psi\rangle = c_1|\phi_1\rangle + c_2|\phi_2\rangle + \cdots c_m|\phi_m\rangle \quad (7)$$

The expectation value for an operator \hat{Q} is given by

$$\langle \hat{Q} \rangle = \langle \psi | \hat{Q} | \psi \rangle = Tr\{|\psi\rangle\langle\psi| \hat{Q}\} \quad (8)$$

Now, consider a system of N spins. The average expectation value of Q is given by summing expectation values for each spin:

$$\begin{aligned} \bar{Q} &= \langle \psi_1 | \hat{Q} | \psi_1 \rangle + \langle \psi_2 | \hat{Q} | \psi_2 \rangle + \cdots + \langle \psi_N | \hat{Q} | \psi_N \rangle \\ &= Tr\{(|\psi_1\rangle\langle\psi_1| + |\psi_2\rangle\langle\psi_2| + \cdots + |\psi_N\rangle\langle\psi_N|) \hat{Q}\} \end{aligned} \quad (9)$$

Let us now define the density operator, $\hat{\rho}$ as follows:

$$\hat{\rho} = \frac{1}{N} [|\psi_1\rangle\langle\psi_1| + |\psi_2\rangle\langle\psi_2| + \cdots + |\psi_N\rangle\langle\psi_N|] = \overline{|\psi\rangle\langle\psi|} \quad (10)$$

Using this operator, the ensemble average of each spin allows \bar{Q} to be determined. Observing a macroscopic system ($N \sim 10^{18}$ spins) will result in a measured value of

$$\bar{Q}_{macro} = N Tr\{\hat{\rho} \hat{Q}\} \quad (11)$$

The average contribution of each spin to the observed quantity is therefore

$$\langle Q \rangle_{spin} = \frac{\bar{Q}_{macro}}{N} = Tr\{\hat{\rho} \hat{Q}\} \quad (12)$$

where the matrix elements of the operator $\hat{\rho}$ are given by $\rho_{ij} = \overline{c_i^* c_j}$, and the ensemble average is taken over all N spins in the ensemble. Physically, the diagonal elements, ρ_{ii} , of the density matrix correspond to the average population of the individual eigenstate $|\phi_i\rangle$. The off-diagonal elements, ρ_{ij} , describe coherent superpositions of the $|\phi_i\rangle$ and $|\phi_j\rangle$ eigenstate. These coherences indicate how the $|\phi_i\rangle$ state is correlated with the $|\phi_j\rangle$ state.

The form of the density matrix can be determined using statistical mechanics. Consider a spin system at thermal equilibrium whose spins are governed by the Hamiltonian \hat{H} . Using the methods of statistical mechanics, we find that

$$\hat{\rho}_{eq} = \frac{1}{Z} e^{-\hat{H}/kT} \quad (13)$$

where Z is the partition function of the system,

$$Z = \text{Tr}\{e^{-\hat{H}/kT}\} \quad (14)$$

and k is Boltzmann's constant. At high temperatures, the density matrix can be approximated as

$$\hat{\rho}_{eq} \approx \frac{1}{Z} \left(\hat{1} - \frac{\hat{H}}{kT} \right) = \frac{\hat{1}}{Z} - \frac{\hat{H}}{ZkT} = \frac{\hat{1}}{Z} + \Delta\hat{\rho} \quad (15)$$

Since the $\hat{1}/Z$ term commutes with applied operators, we may express the density matrix in terms of the deviation density matrix, $\Delta\hat{\rho} = -\hat{H}/ZkT$. In NMR experiments, we can therefore treat our pulses as operators applied to the deviation density matrix (see Section 2.4).

Since the elements of the density matrix depend solely on the average properties of the spin system, the use of the density operator allows us to completely characterize an ensemble of spins with a single ($m \times m$) matrix. For systems at thermal equilibrium, a complete description is possible using only the Hamiltonian of an individual spin.

2.4 The Pulse Operator

Using the density matrix, we can evaluate the effect of radiofrequency NMR pulses on the spin ensemble. Consider a pulse described by Hamiltonian \hat{H}_p which interacts with the spin ensemble. The change in the density matrix caused by the pulse is given by the Liouville-von Neumann equation:

$$\frac{d\hat{\rho}}{dt} = -i[\hat{H}_p, \hat{\rho}] \quad (16)$$

Solving this differential equation, we find that

$$\hat{\rho}(t) = e^{-iH_p t/\hbar} \hat{\rho}(0) e^{iH_p t/\hbar} \quad (17)$$

To describe a sequence of pulses, we can simply add additional exponential pulse operators to either side.

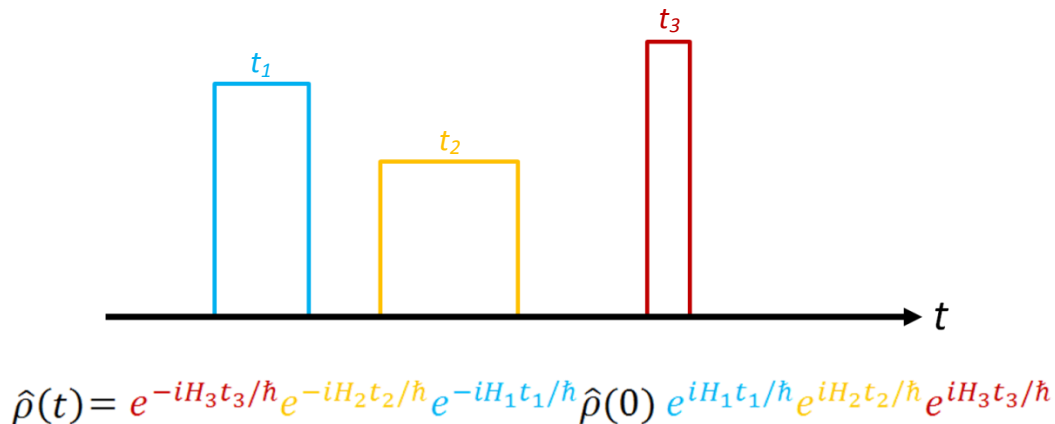


Figure 3: The effect of an arbitrary sequence of radio frequency pulses on the density matrix of a system may be calculated by “sandwiching” exponential pulse operators for each pulse on either side of the density matrix. These operators are generally non-commuting; as such, the order in which they are applied is significant.

The density matrix representation of a spin ensemble is extremely powerful: if we know the Hamiltonian describing the interaction of the pulse (\hat{H}_p) and the Hamiltonian describing a single spin within a spin system (\hat{H}), we can calculate the density matrix of the system’s initial state, $\rho(0)$, as well as the state of the system after an arbitrary sequence of pulses. In NMR experiments, the “pulse” which disturbs the density matrix is a radiofrequency pulse applied perpendicularly to the static applied field. (If

this field is taken to be along the z -axis, then the pulses are applied in the x - y plane. The Hamiltonian of this interaction is given by:

$$H_p = -\hbar(\omega_{RF} - \omega_0)I_z - \hbar\omega_1 I_\alpha + \frac{\hbar\omega_Q}{3}(3I_z^2 - I(I+1)) \quad (18)$$

where $\omega_1 = \gamma B_1$ gives the strength of the applied RF pulse in terms of the RF pulses' amplitude, B_1 , and I_α gives is the operator for the α th component of the spin angular momentum [5].

2.5 “Spin Response” – A Method of Simulating Pulse Sequences

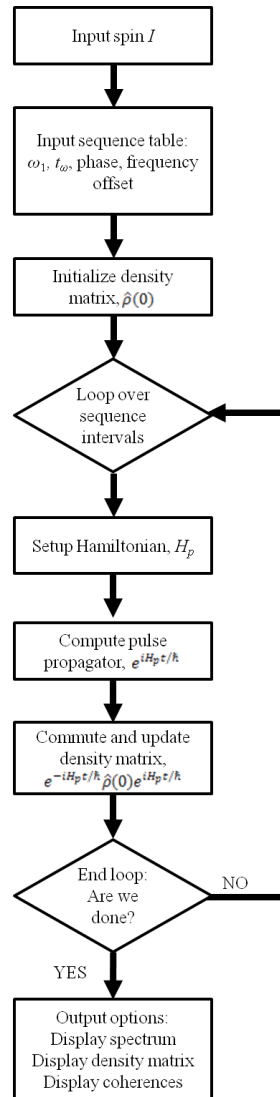


Figure 4: Flow diagram of Spin Response program.

Using the density matrix formulation of NMR in conjunction with the exponential pulse operators, it is straightforward to calculate the density matrix and coherences for a collection of spins after an NMR experiment.

Dr. Robert Vold has written a program in MatLab, entitled “Spin Response” (SR), which uses Eqs. 5, 15-18 to calculate the density matrices and coherences a spin-3/2 or spin-7/2 nuclei after an arbitrary, user-specified sequence of RF pulses. Using the elements of the density matrix, the program is also able to simulate the NMR spectra corresponding to that sequence of pulses. A flow diagram describing the operations performed by the program is given in Fig. 4. Using SR, I was able to simulate the NMR spectra corresponding to each of my experimental pulse sequences. The provided a basis of comparison for my experimental spectra.

2.6 NMR As A Quantum Computing Method

2.6.1 Basics of Quantum Computing

With the basics of NMR spectroscopy and the formalism of the deviation density matrix in place, we can now discuss the fundamentals of quantum computing. In a conventional computer, information is encoded in binary bits, which can occupy either a “1” or a “0” state. In a quantum computer, quantum particles are used as quantum bits (“qubits”). These qubits can occupy the binary 1 and 0 states of the traditional computer, as well as any quantum superposition of these two states. A spin-1/2 particle used as a qubit, for instance, can occupy the spin down state, $|1\rangle$, the spin up state, $|0\rangle$, as well as a superposition of the two states, $\psi = c_0|0\rangle + c_1|1\rangle$.

Once information is encoded in qubits, quantum logic gates are used to manipulate the stored state. These gates can then be combined to create quantum algorithms. One of the most basic quantum logic gate, the controlled NOT (“CNOT”) gate, changes the state of a target qubit based on the state of a control qubit. If the control qubit has a value of 1, the target qubit’s state is changed. If the control qubit is 0, the target qubit’s state remains unchanged. The truth table for this logic gate is given below:

Table 2: Truth Table of CNOT Logic Gate

X	CNOT(X)
00⟩	00⟩
10⟩	11⟩
01⟩	01⟩
11⟩	10⟩

Table 2: Truth diagram for the CNOT gate applied to a two qubit system. Here the first qubit acts as the control qubit, and the second qubit acts as the target qubit.

2.6.2 NMR as a Quantum Computing Method

The tools of NMR spectroscopy allow for the precise creation and manipulation of quantum spin states, making NMR an ideal platform for quantum computation. The quantum registers used in NMR generally take one of two forms. In the first configuration, a network of several coupled spin-1/2 nuclei (such as carbon-13 or protons). Each nucleus acts as a single qubit, which can be independently selected by tuning the NMR signal to the appropriate resonant Larmor frequency.

In the second configuration, the energy levels of a quadrupolar nucleus serve as the quantum register. As discussed previously (see Section 2.2), the quadrupolar interaction of the nucleus and the electric field gradient result in non-uniform perturbations of the nuclei's Zeeman energy levels. Since the energy levels are no longer evenly spaced, specific transitions between energy levels can now be excited using selective NMR pulses, allowing us to populate specific energy levels. Each of these energy levels corresponds to some combination of spin-1/2 qubits. A spin-3/2 nucleus, for example, has four energy levels, each of which correspond a combination of two spin-1/2 qubits. As such, the energy levels are labeled |11⟩, |10⟩, |01⟩, and |00⟩ (see Fig 5). A spin-7/2 nucleus has eight energy levels, each of which can represent a combination of three spin-1/2 qubits. In general, a quadrupolar nucleus with spin $I = \frac{1}{2}(2^N - 1)$ has energy levels corresponding to combinations of N spin-1/2 qubits.

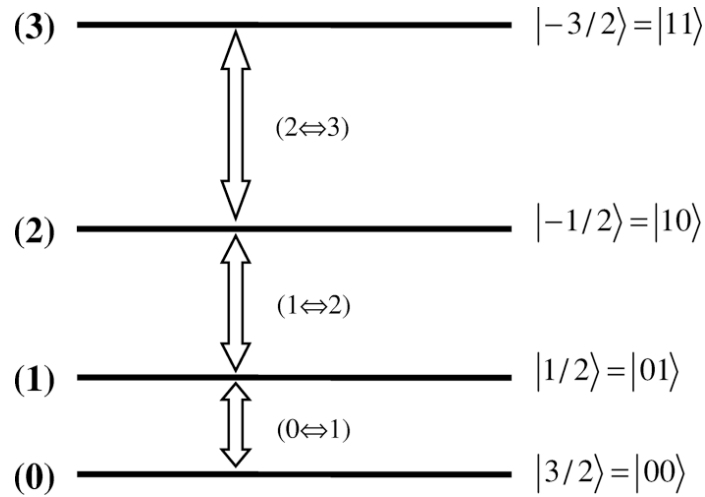


Figure 5: The energy levels of a spin-3/2, quadrupolar nucleus. Each of the four energy levels corresponds to a combination of spin-1/2 qubits. The $m_l = -3/2$ energy level, for instances, corresponds to two spin-1/2 qubits in the 1 state. We label this state $|11\rangle$ [3].

Quantum algorithms are defined by specific sequences of radiofrequency pulses. These pulses manipulate the populations and the coherences of the system's energy levels, transforming the system's initial state into some final state. This final state can be determined by taking a Fourier transform of the resulting readout signal, which gives an NMR spectrum. However, since the same spectrum can describe multiple density matrices, the final state can be checked more precisely using quantum tomography, a technique which uses specially designed pulse sequences to independently measure each element of the density matrix [3], [5].

3. Experiment

The experimental portion of our project consisted of four main parts: first, we prepared a lyotropic liquid crystal solution of sodium decyl sulfate, deuterium oxide, and decanol, which would act as a two qubit register. We then optimized $\pi/2$ and π selective and nonselective pulses for each of the three single quantum transitions in our spin system. Using sequences of these selective pulses, we created pseudopure initial states. The diagonal elements of the density matrices for these states were read out using a non-selective, $\pi/20$ pulse. Finally, we applied a CNOT logical gate to these pseudopure states and reproduced results from the literature [6].

3.1 Experimental Set-Up

Our NMR experiments were performed using Small Hall's 17.6 T Bruker Avance I spectrometer. Data was taken using a Bruker static, non-spinning 5 mm probe near room temperature, at temperatures between 290K and 300K. Stable sample temperatures were maintained using a Bruker temperature control unit (BCU 05), which kept sample temperatures constant to within 0.1 K. Our experiments use a thermotropic liquid crystal as a quantum register. Fluctuations in temperature can change the state of the sample – precise temperature regulation is therefore important to ensure the crystal remains in a nematic phase.

3.2 Preparation of Liquid Crystal Sample

Our NMR experiments were performed in the nematic phase of a lyotropic liquid crystal solution composed of sodium decyl sulfate dissolved in a mixture of deuterium oxide and decanol. In this phase, the long decyl chains align parallel to a preferred axis (see Fig. 6).

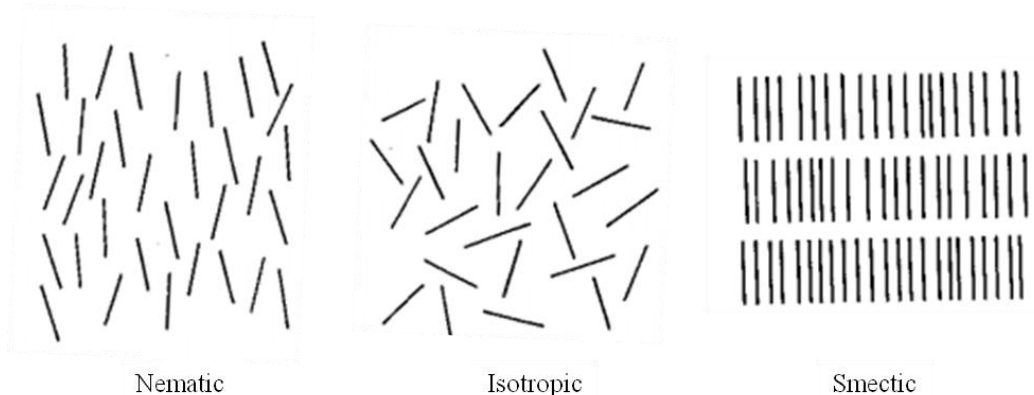


Figure 6: Basic phases of a liquid crystal. In the nematic phase (left), molecules have long-range orientational order in a preferred direction, but lack long-range translational order. In the isotropic phase (center), there is no long range or short range order in any direction. In the smectic phase (right), molecules form layered structures, with each layer featuring a unique structure. [7].

While the ions are free to move throughout the sample, they maintain their long-range alignment, resulting in narrow, evenly spaced NMR spectral lines. This separation of spectral lines (~15 kHz) allows for the easy application of selective pulses.

With the help of Dr. Christopher Abelt of the chemistry department, I prepared a solution of sodium decyl sulfate ($\text{CH}_3(\text{CH}_2)_9\text{OSO}_3\text{Na}$, also known as SDS) and decanol in deuterium oxide (D_2O). Each of the three compounds was weighed out separately, and then combined in a test tube. (The weight percentages of each component are given in Table 3 below. The concentrations used are the same as those used by Bonk, et. al. [5].) The concentration of each material proved to be very important: in an early attempt to produce the solution, some of the SDS was lost during the mixing process. As a result, we were unable to produce a nematic phase in that particular sample.

The solution was then mixed in several steps: first, a magnetic stir bar was placed into the sample, and mixing was done using a magnetic stir plate. To ensure all the SDS was dissolved in solution, the sample was warmed with a heat gun, and then placed into a sonicator, where it was further mixed. These steps were repeated in various permutations until we were certain that the sample was homogeneous.

Table 3: Liquid Crystal Composition

Compound	Weight Percentage
SDS	20.92%
Decanol	3.78%
D ₂ O	75.40%

This sample was placed in a 5 mm diameter NMR tubes about 1.25 cm in length. These tubes were closed with a plastic cap, which was wrapped with a layer of parafilm.

To determine the temperature at which the nematic phase occurred, we warmed the sample to the isotropic phase. This phase transition occurs at approximately 320 K. After waiting for the sample come to thermal equilibrium at this temperature (a wait time of between 15 min to an hour), the sample was cooled down to a final temperature. After waiting 1 – 3 hours for the sample to reach equilibrium, we took an NMR spectra to see if the sample had reached a nematic phase. (A longer wait is necessary to ensure that the sample has reached thermal equilibrium, and that all the molecules have reached their preferred orientation, producing the nematic phase.) This process was repeated for final temperatures between 280 K and 305 K, with measurements taken every 0.5 K. We found the nematic phase occurred between 290 K and 300 K. The maximum peak intensity for the side peaks occurred between 290 K and 295 K.

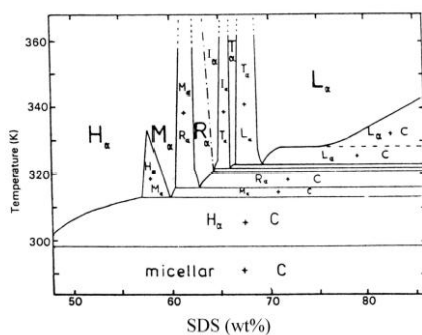


Figure 7: Sample phase diagram for an SDS liquid crystal. Notice the complicated dependence of the crystal phase on SDS concentration and temperature [8].

While creating this liquid crystal solution should have been easiest part of my project, this step took the longest amount of time to complete. In general, the nematic phase of a thermotropic liquid

crystal remains stable at a fixed temperature. The behavior of our sample, however, appeared to change over time. NMR experiments performed soon after the sample was placed in the magnet produced three distinct, narrow lines, with peak widths on the order of 100 – 300 Hz. However, after several weeks, the outer two spectral lines had slowly decreased in amplitude and broadened to around 1 kHz in width - too wide to be selectively excited. In some instances, the side peaks would eventually disappear. This change of peak width as a function of time is shown in Fig. 8 below.

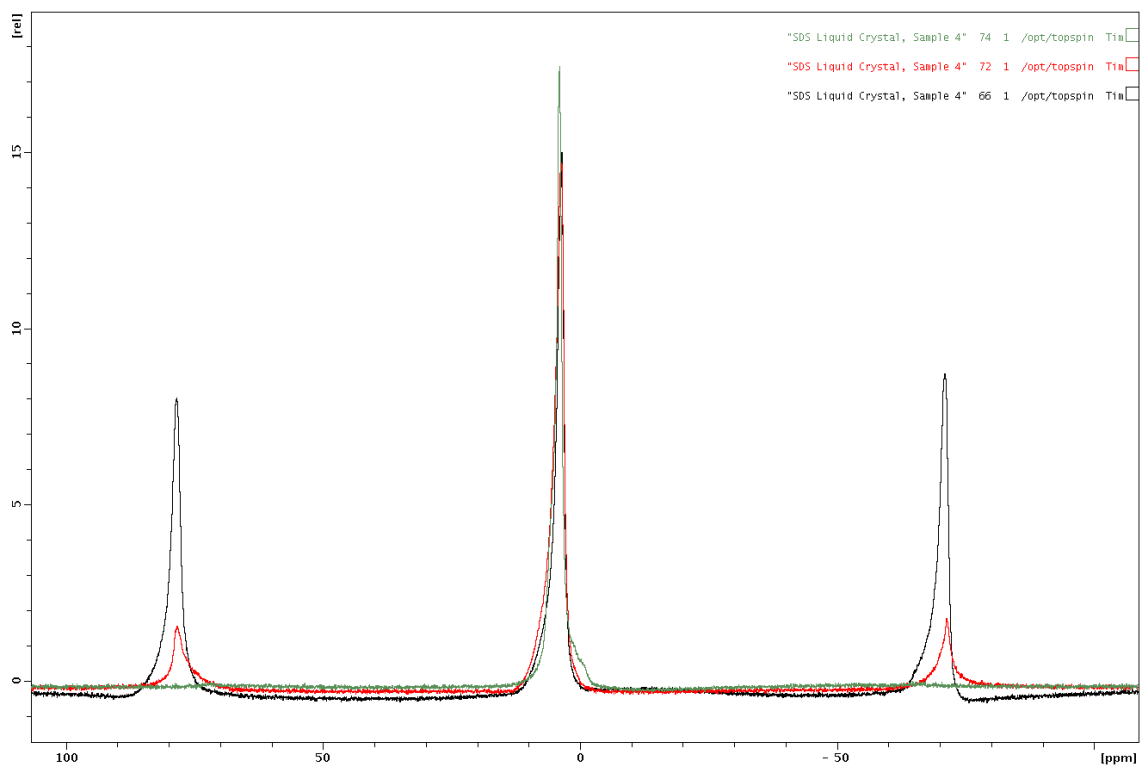


Figure 8: Na-23 NMR spectra of SDS liquid crystal at 293 K. For each spectra, the pulse length is $6.75 \mu\text{s}$ and the power level is 30 dB. Spectra were taken on 4/7/14 (black), and the next morning, 4/8/14 (red, green). This change in peak intensity may be the result of the evaporation of solvent from the sample, leaks in the sample tube, or movement of the sample within the sample tube. These are discussed further below.

Initially, we believed that the sample was not in a stable nematic phase. Liquid crystals often have complex phase diagrams (see Fig. 7), so perhaps my sample was in some combination of nematic and smectic phases. To better characterize the sample's changing state, we recorded NMR spectra every 0.5 K for temperatures between 280K and 300K. In this way, I hoped to locate a temperature at which the

sample was in a stable nematic phase. While we measured some dependence of peak intensity and width on temperature, we were unable to coax the system into a stable phase – no matter the temperature, the side peaks would eventually widen and disappear

During our phase characterization experiments, we noticed that the volume of the sample within the tube appeared to be slowly decreasing with time. Initially, we believed that this was the result of leakage from the sample tube. However, a thorough examination of the probe revealed no wet areas or other evidence of a leak. Additionally, taking a spectrum with the probe empty did not indicate any leaked sample inside the probe's pick-up coil. While our scans revealed a small (less than 5% of peak amplitude) background signal, this signal was still present after the probe was thoroughly cleaned. Additionally, the signal appears in the background of experiments prior to the suspected leak, and it can be removed entirely using a background-suppressing pulse sequence, leading us to believe that the signal is an artifact of some background signal rather than evidence of a leak. Another explanation for the change in peak width was the slow evaporation of solvent from the sample tube. While this explanation is consistent with our results, all our experiments were run at temperature between 280 K and 320 K, well below the boiling point of D₂O (374.5 K). As such, we expect the change in peak width to occur over a longer time scale – perhaps over a month instead of one or two weeks.

Another possible source of this time-dependent line broadening is the viscous liquid crystal slowly moving inside the sample tube. When the liquid crystal is placed inside the tube, the liquid crystal is entirely at one end of the tube. However, as the tube sits on its side, the sample slowly shifts from the end of the tube to along its side. The slow movement of the liquid crystal produces a large interface between the sample and air inside the tube. This air-liquid crystal interface could result in a diamagnetic susceptibility anisotropy, which could then interfere with the homogeneity of the external magnetic field and the applied rf pulses, ultimately resulting in a widening of the peaks of our NMR spectra.

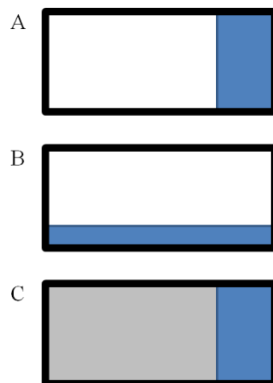


FIGURE 9: When the liquid crystal (shown in blue) is initially placed in the sample tube, the sample tends to stay in the end of the sample tube (A). As time passes, however, the liquid crystal moves down from the side, spreading along the bottom of the sample tube. This increases the size of the crystal-air interface, resulting in magnetic field inhomogeneities around the sample (B). Using a wax stopper (grey), we force the sample to remain in one end of the tube. This reduces sample movement, and has the added benefit of preventing any leaks (C). In all cases, the sample tube is placed with the sample in the center of the probe's pick-up coil.

In an attempt to eliminate all these possible sources of peak broadening, we sealed the sample by dripping melted paraffin wax onto the end of the sample tube. This melted wax should form an airtight seal, which would stop (or at least slow) any leaks or solvent evaporation. The wax has the added benefit of keeping the liquid crystal from moving around inside the sample tube.

While the addition seemed to increase the stability of the nematic phase, some fluctuations in the resulting NMR spectra were still observed. After several weeks of relative stability, the side peaks of the NMR spectra disappeared overnight, in spite of the wax seal. While we were able to recover the peaks by removing the sample from the magnet, warming it, and then replacing it in the magnet, we were unable to recover the full amplitudes of the side peaks. The amplitude and width of the peaks, however, proved sufficient for selective excitations, thus allowing for the implementation of quantum computations (see Fig 10 and Section 3.3).

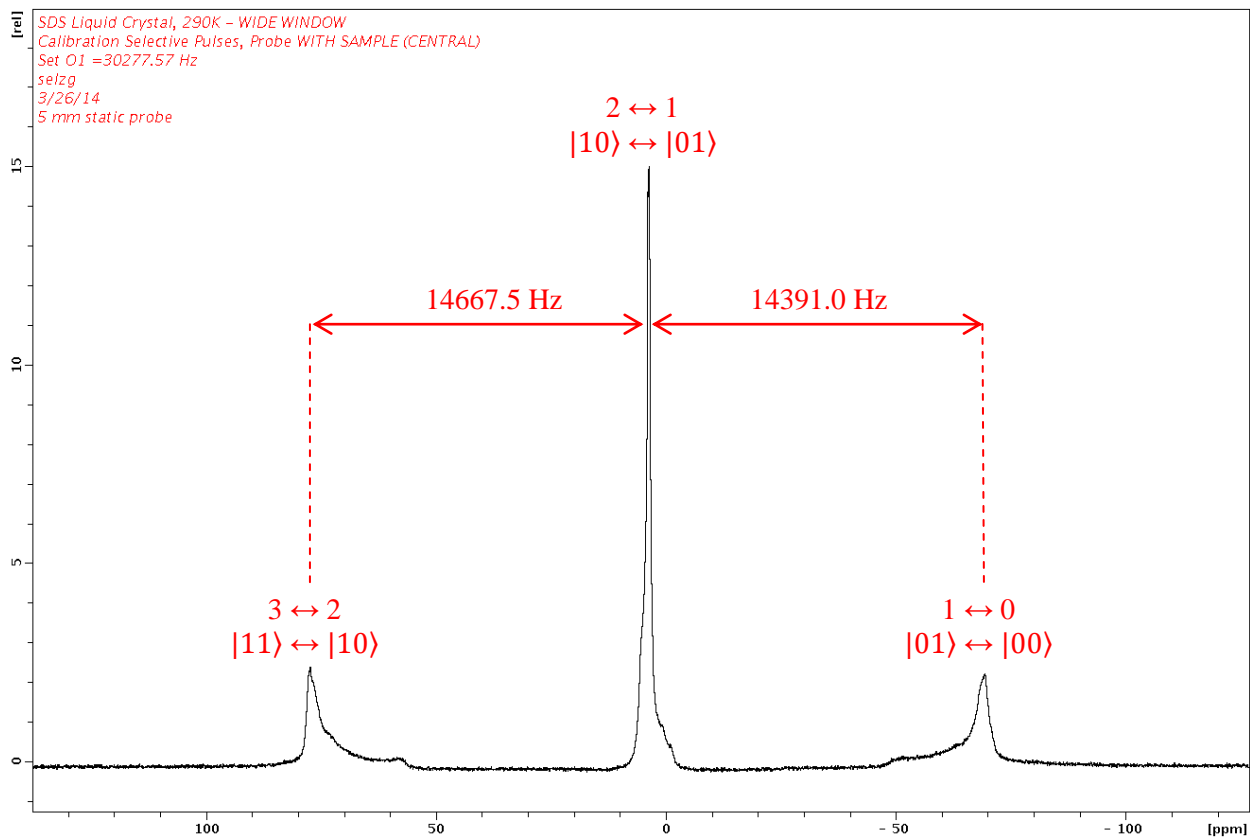


Figure 10: Na-23 NMR spectrum of SDS liquid crystal. Peaks separation is 14 kHz. The left and right peaks have full widths at half max widths (FWHM) of 580 Hz and 620 Hz, respectively. The central peak has a FWHM of 175 Hz. Each transition is labeled using the numbering of Fig. 5.

3.3 Calibration of Selective Pulses and Creation of Pseudopure States

With the liquid crystal finally oriented reproducibly, I calibrated $\pi/2$ and π selective pulses for each of the three peaks. To increase selectivity, we used shaped Gaussian pulses with a very lower power level (30 dB). The pulse frequency was adjusted to match the desired energy transition. Using Topspin's POPT command, we measured the intensity of each peak as a function of pulse length. POPT works by linearly varying a particular parameter of the pulse sequence, in this case the pulse length, and taking an NMR spectrum for each value of the parameter (see Fig. 11).

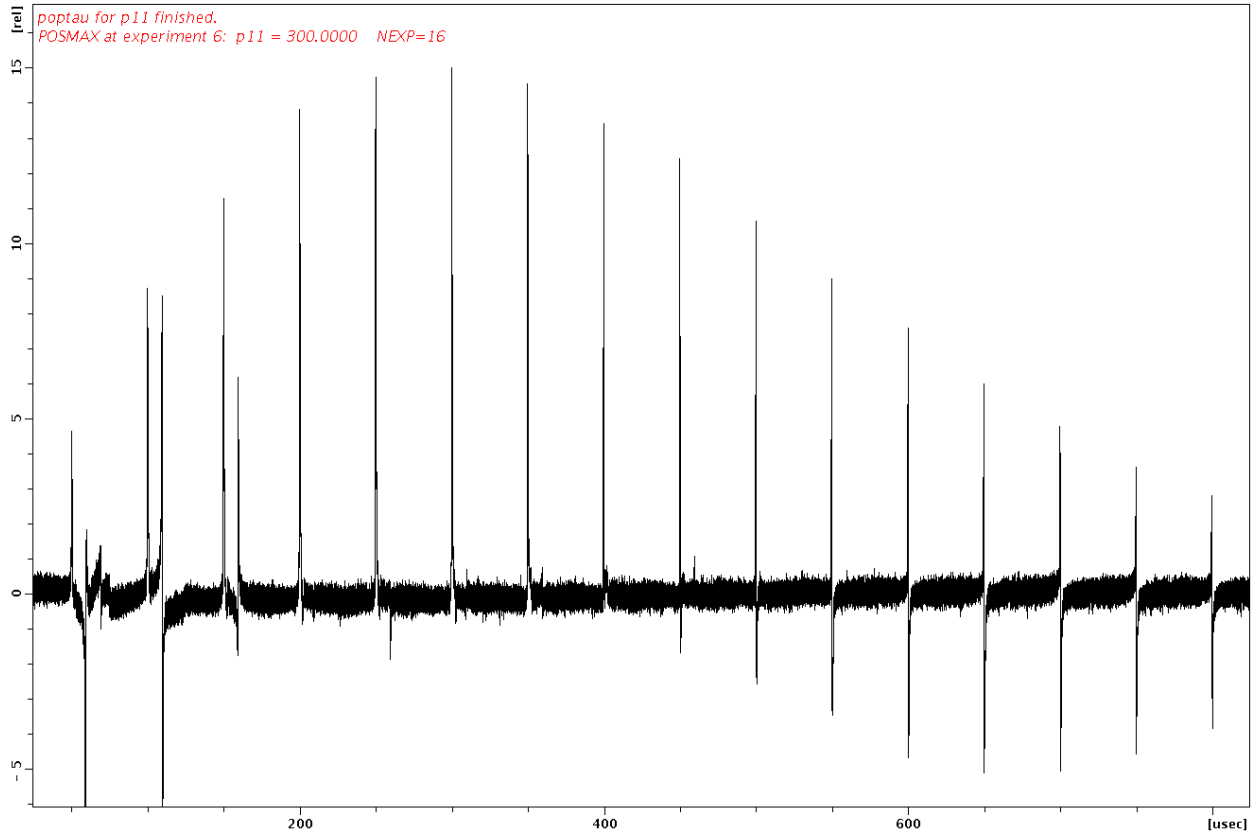


Figure 11: A sample POPT optimization for the $\pi/2$ pulse length for a selective pulse along the central transition. The pulse length varies between $50 \mu\text{s}$ and $800 \mu\text{s}$, in $50 \mu\text{s}$ increments. The spectra for each pulse length are displayed one after the other. Here the $\pi/2$ pulse length occurs at $300 \mu\text{s}$. The π pulse length occurs at around $800 \mu\text{s}$.

The $\pi/2$ pulse lengths were found by visually identifying the pulse length which maximized the selected peak and minimized the other peaks. The π pulse length was given by visually identifying the value of p11 which minimized all three peaks.

This process, however, was complicated by the dynamic behavior of our sample discussed above. While we were able to calibrate the selective pulse lengths easily enough, our calibrations would change with the varying amplitudes and widths of the three peaks. As such, separate calibrations had to be performed each time we noticed that the peaks had shifted or whenever the sample was removed from the probe. We were, however, able to determine a range of pulse lengths corresponding to the $\pi/2$ and π selective pulses for each peak. While most of these variations were on the order of $30 \mu\text{s}$ to $40 \mu\text{s}$, the

pulse lengths for the central transition varied and the π pulse for the right transition varied by hundred of microseconds. The measured ranges are given below:

Table 4: Range of Expected Pulse Lengths

Transition	Pulse Type	Length Range (μs)
2 \leftrightarrow 3 11> \leftrightarrow 10> (Left Peak)	$\pi/2$	210 – 250
2 \leftrightarrow 3 11> \leftrightarrow 10> (Left Peak)	π	470 – 575
1 \leftrightarrow 2 10> \leftrightarrow 01> (Center Peak)	$\pi/2$	250 – 375
1 \leftrightarrow 2 10> \leftrightarrow 01> (Center Peak)	π	440 – 800
0 \leftrightarrow 1 01> \leftrightarrow 00> (Right Peak)	$\pi/2$	200 – 450
0 \leftrightarrow 1 01> \leftrightarrow 00> (Right Peak)	π	490 - 950

Table 4: Optimized experimental pulse lengths for selective pulses on each transition. Here we use Fig. 5's labeling for energy levels.

Using these ranges of pulse lengths, we were able to produce pseudopure states. In a pseudopure state, the configuration of the deviation density matrix corresponds to a pure state. According to the literature [6], pseudopure states may be produced using the following pulse sequences:

Table 5: Pulse Sequence Used To Generated Pseudopure States [6]

Pseudopure State	Pulse Sequence
00>	$(\pi)_{12} - (\pi/2)_{23}$
01>	$(\pi)_{12} - (\pi/2)_{23} - (\pi)_{01}$
10>	$(\pi)_{12} - (\pi)_{23} - (\pi/2)_{01}$
11>	$(\pi)_{12} - (\pi/2)_{01}$

Here $(x)_{\alpha\beta}$ represents a selective pulse along length x applied to the $\alpha \rightarrow \beta$ energy transition. Off-diagonal elements of the density matrix may be suppressed by applying a gradient pulse after the appropriate pulse sequence is performed. Instead of using gradient pulses, we used phase cycling to cancel out undesired coherences. π pulses were phase cycled between $(x, -x)$, and $\pi/2$ pulses were cycled

between $(x, -x, y, -y)$. After each pulse sequence, a hard $\pi/20$ pulse with power level 0 dB and length $0.54 \mu s$ was used to measure the state of the system.

Using SR, we may simulate each of these pulse sequences to ensure that they produce the expected pure states. These simulations are given in Figs. 12-15 below:

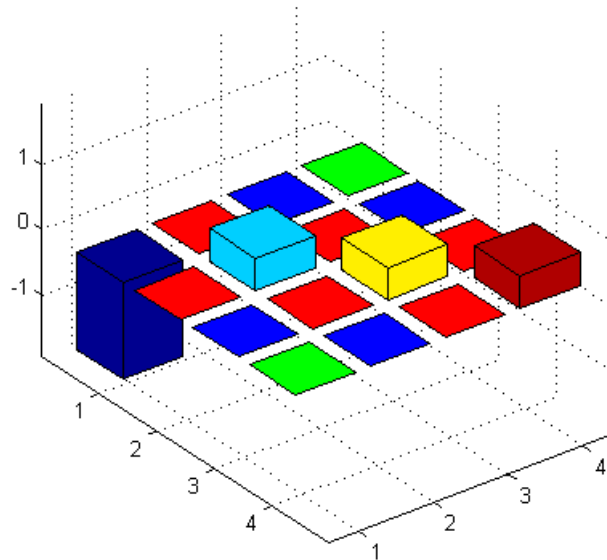


Figure 12: SR simulation of density matrix elements for the $(\pi)_{12} - (\pi/2)_{23}$ pulse sequence. We see that this pulse sequence produces a $|00\rangle$ pseudopure state.

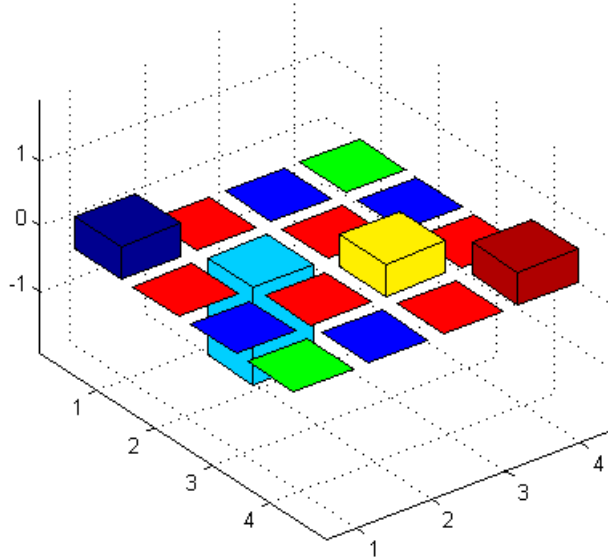


Figure 13: SR simulation of density matrix elements for the $(\pi)_{12} - (\pi)_{23} - (\pi/2)_{01}$ pulse sequence. We see that this pulse sequence produces a $-|10\rangle$ pseudopure state.

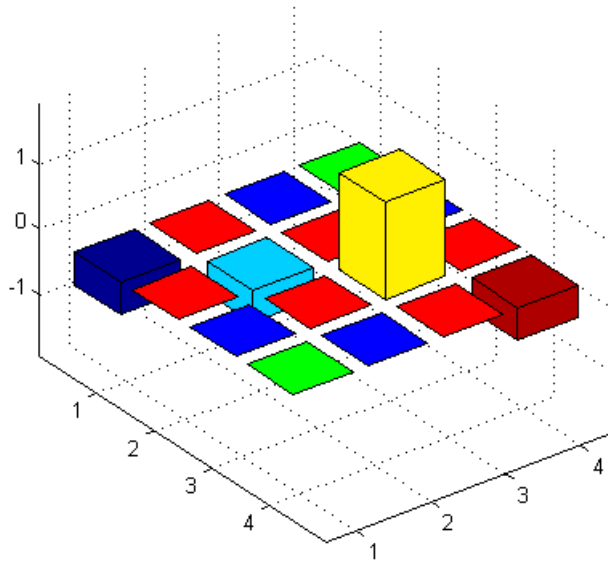


Figure 14: SR simulation of density matrix elements for the $(\pi)_{12} - (\pi)_{23} - (\pi/2)_{01}$ pulse sequence. We see that this pulse sequence produces a $|10\rangle$ pseudopure state.

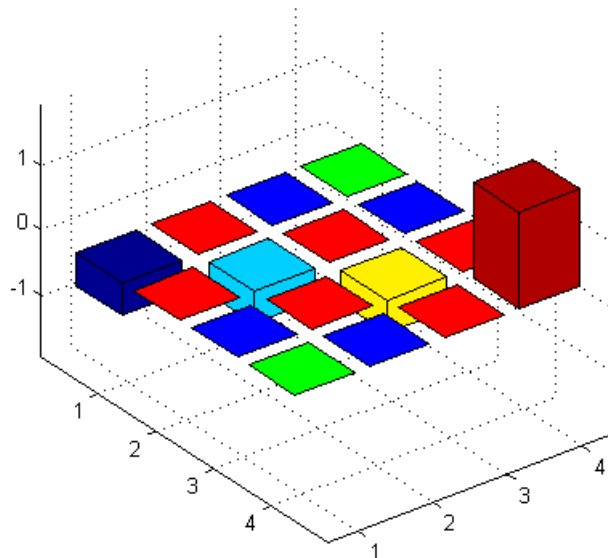


Figure 15: SR simulation of density matrix elements for the $(\pi)_{12} - (\pi/2)_{01}$ pulse sequence. We see that this pulse sequence produces a $|11\rangle$ pseudopure state.

Each of these pulse sequences was programmed using Topspin's pulse programmer – the code for each of the pulse sequences is given in the Appendix. Graphically, the pulse sequence can be represented in the form of Fig. 16:

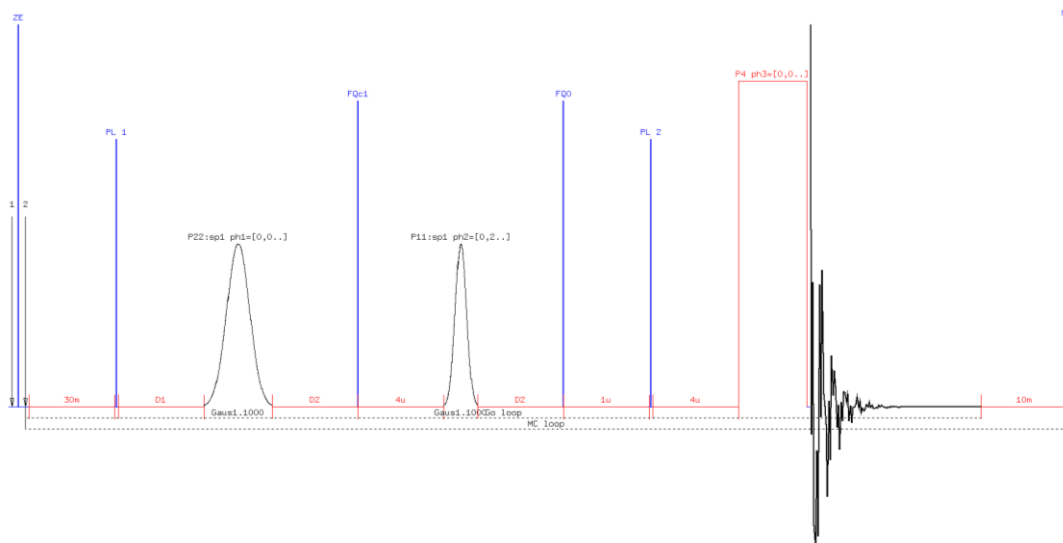


Figure 16: This figure gives a pictorial representation of the pulse sequence used to produce the $|00\rangle$ state. This pulse sequence consists of two selective Gaussian pulses. The first is a π pulse applied along the central transition. After $(D2 + 4) \mu s$, a $\pi/2$ pulse applied along the left transition. After another $(D2 + 5) \mu s$, a hard $\pi/20$ nonselective pulse is used to read out the NMR spectrum. This sequence is then repeated a user-specified number of times (typically $N = 128$ in our experiments), with the phase of each pulse cycled appropriately. (Note that in this diagram, the pulses are not drawn proportional to their lengths. The two Gaussian pulses are between 250 and 500 μs , whereas the hard readout pulse is 0.5 μs .)

The pulse sequences corresponding to each pseudopure state were optimized using repeated applications of the POPT command. First, an initial spectra was taken using estimated pulse lengths with the appropriate ranges. Using POPT, we then determined an exact pulse length which would minimize or maximize the corresponding peak within the spectrum. This process was repeated for each pulse in the sequence. For instance, in the $|00\rangle$ state, we apply a π pulse along the central peak, and a $\pi/2$ pulse to the left-hand peak. However, we only expect the right peak to appear in the resulting spectrum. We therefore use POPT to find the length of the $(\pi)_{12}$ pulse which minimizes the central peak. We then perform then perform a second POPT to find the $(\pi/2)_{23}$ pulse length which minimizes the left-hand peak. Since the pulse length of one peak in a sequence may change the optimum values of other pulses within the sequence, we repeated the optimization process until small changes in the optimal value for each pulse did not change the spin response of the system. The spectra corresponding to each of the pseudopure states are given in Section 4.

3.4 Implementation of Quantum CNOT Gate

The set of pseudopure states described in the previous section can now be used to test quantum logic gates. We now consider the CNOT gate (see Table 2). In NMR, this gate can be represented by a single, selective $(\pi)_{23}$ pulse applied along the x -axis at the frequency of the $2\leftrightarrow 3$ (that is, the left) transition [3]. To apply this gate to a given pseudopure state, we simply add it to the appropriate pulse sequence for that state. The pulse corresponding to the logic gate is placed between the sequence of pulses which generates the initial state and the $\pi/20$ reading pulse, as seen in Fig. 17 below:

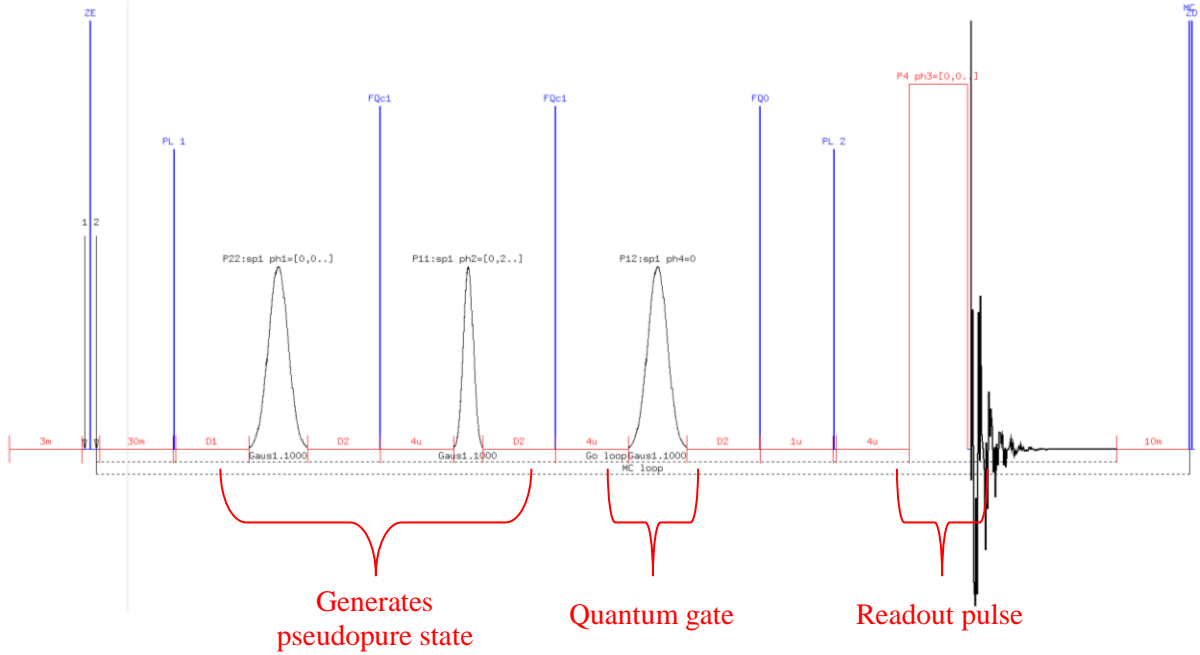


Figure 17: This figure gives a pictorial representation of the pulse sequence used to apply the CNOT gate to the $|00\rangle$ state. The sequence is identical to Fig. 16, with the addition of a selective $(\pi)_{23}$ pulse applied in the x direction placed between the first two selective pulses and the hard readout pulse.

Using this pulse program, we applied a CNOT gate to the four initial states produced above. The optimum length of the $(\pi)_{23}$ pulse was found using the POPT command, and was taken to be $P_{11} = 520 \mu\text{s}$. As with the other selective pulses, the intensity of this pulse was very low to ensure selectivity (30 dB). The resulting spectra are given in Section 4.

Lastly, as an addition test of our CNOT gate pulse sequences, we applied a set of two CNOT gates to each of the four pseudopure states. Applying the CNOT gate twice for a given state should return the initial state (see Table 2.).

4. Discussion

Using the pulse sequences in Table 5, we produced the four possible pseudopure states for a spin-3/2 nuclei. The spectra for each pure state very nearly matches the spectra given in the literature (see Fig. 18), but with some residual amplitude in several peaks which we expect to remain unexcited. This may be indicative of imperfect phase cycling: if our phase cycling did not perfectly cancel the off-diagonal elements of the deviation density matrix, then these coherences may contribute to the resulting NMR spectra, resulting in unexpected peak excitations. Additionally, these residual amplitudes may be the result of imperfect pulse selectivity. However, given our thorough optimization of each selective pulse, this seems unlikely. Since the amplitudes of these unexpected features are small compared to the expected spectra, I am confident that we have obtained the correct pseudopure states (see Figs. 19 – 22 below.)

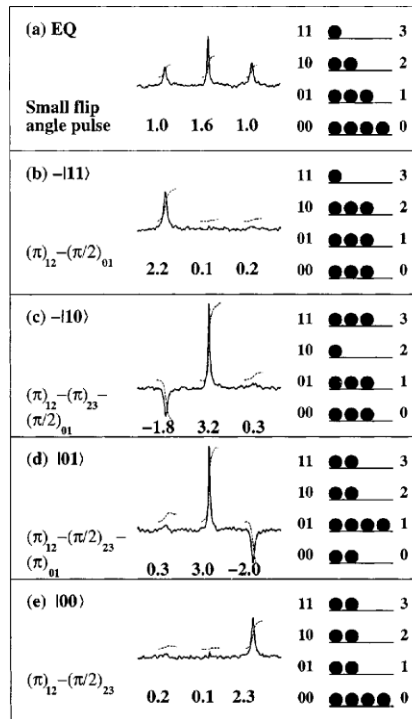


Figure 18: Expected spectra for each pseudopure state, as given by Sinha [6].

Applying the CNOT quantum gate to a given pseudopure state A will produce another pseudopure state, which we can call $\text{CNOT}(A)$. For instance, if CNOT is applied to the $|11\rangle$ state, we obtain

$\text{CNOT}(|11\rangle) = |10\rangle$ (see Table 2). To check the purity of the pseudopure initial state, we can compare $\text{CNOT}(A)$ with the corresponding pseudopure state A . These comparisons are given in Figs. 19-22 below:

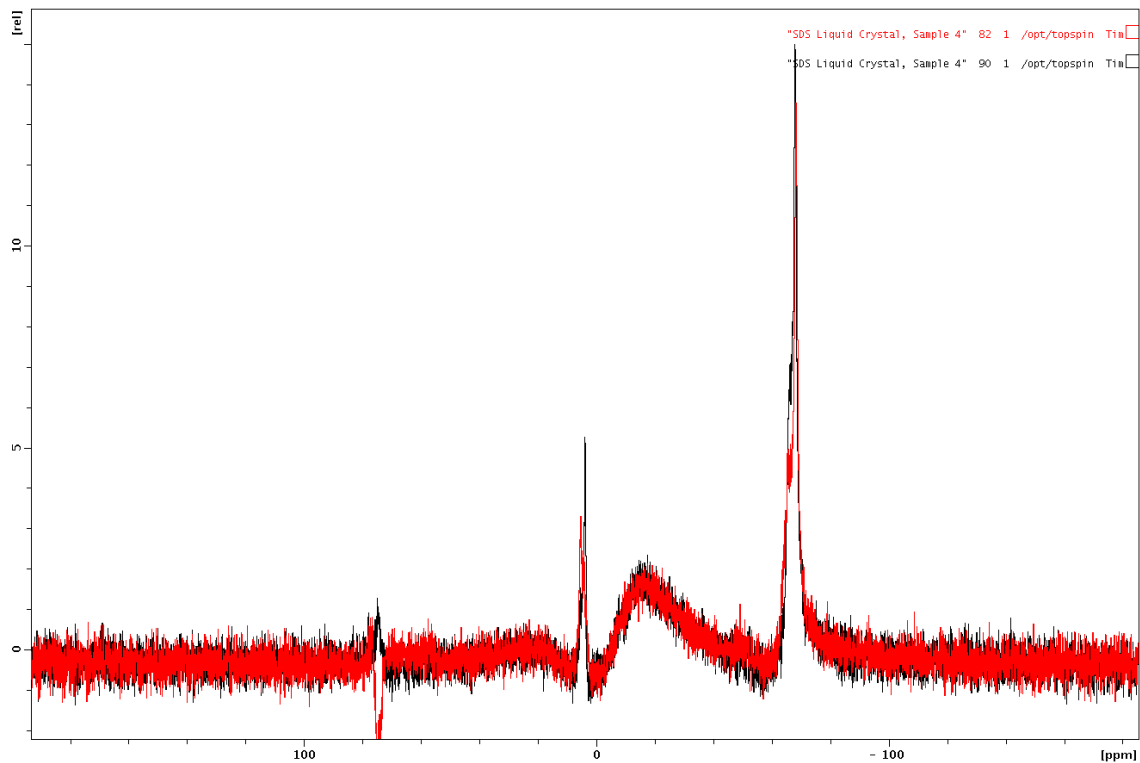


Figure 19: $\text{CNOT}(|00\rangle\rangle$ state (black) and $|00\rangle$ pure state (red). While the application of the CNOT gate changes the phase of the left peak, this peak is still minimized. The application of the CNOT gate produces the expected final state.

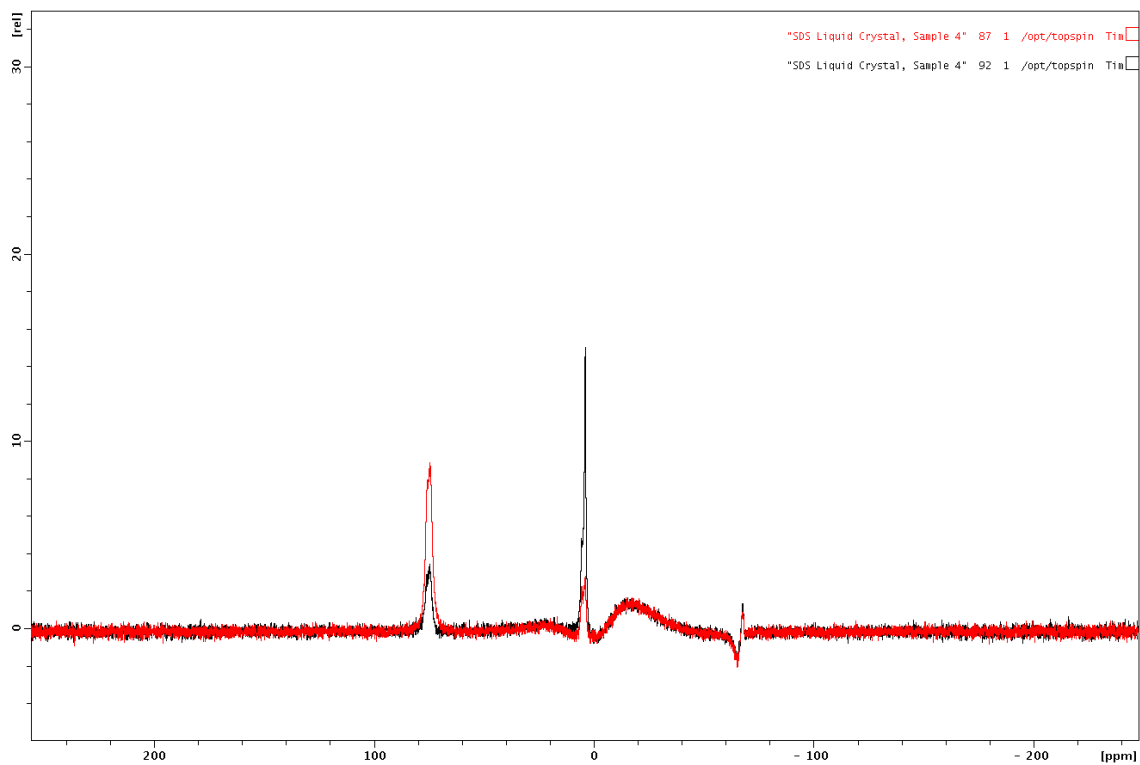


Figure 20: CNOT($|10\rangle$) state (black) and $|11\rangle$ pure state (red). The application of the CNOT gate does not appear to have produced the expected final state. Instead, it has excited the central peak, and has weakly excited the left transition. The right transition appears unchanged by the CNOT gate.

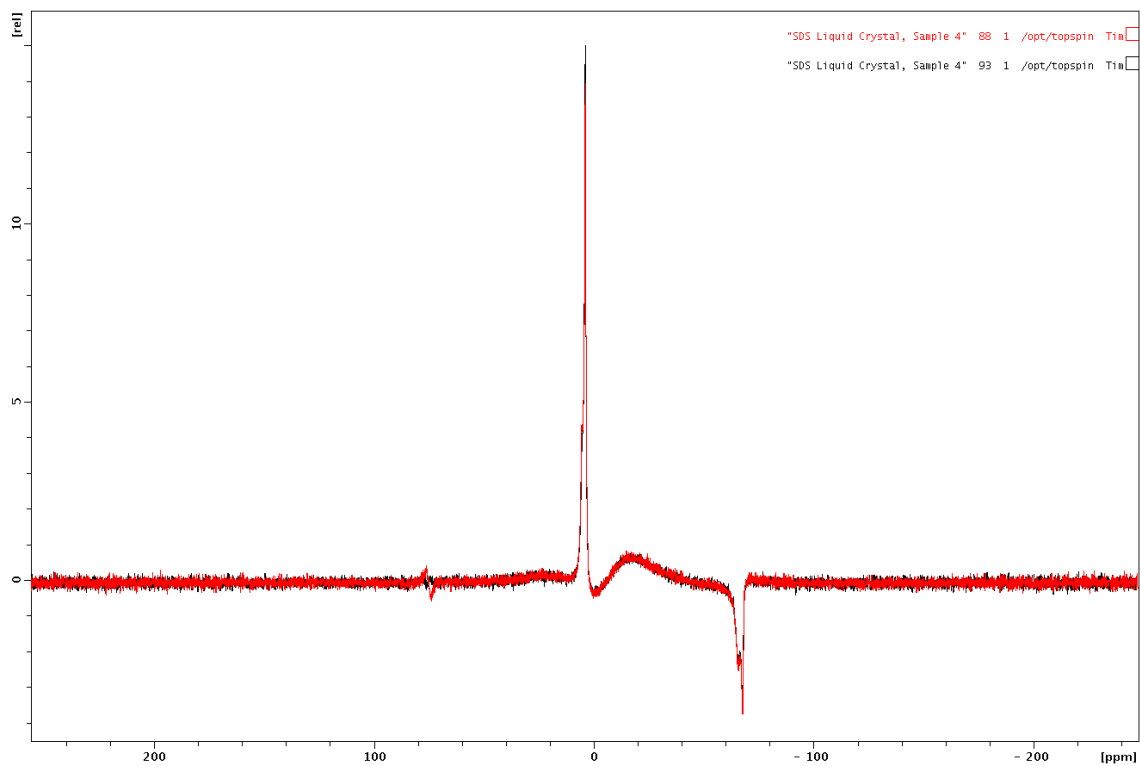


Figure 21: CNOT($|01\rangle$) state (black) and $|01\rangle$ pure state (red). The application of the CNOT gate has excited the left transition slightly, but has produced the expected final state.

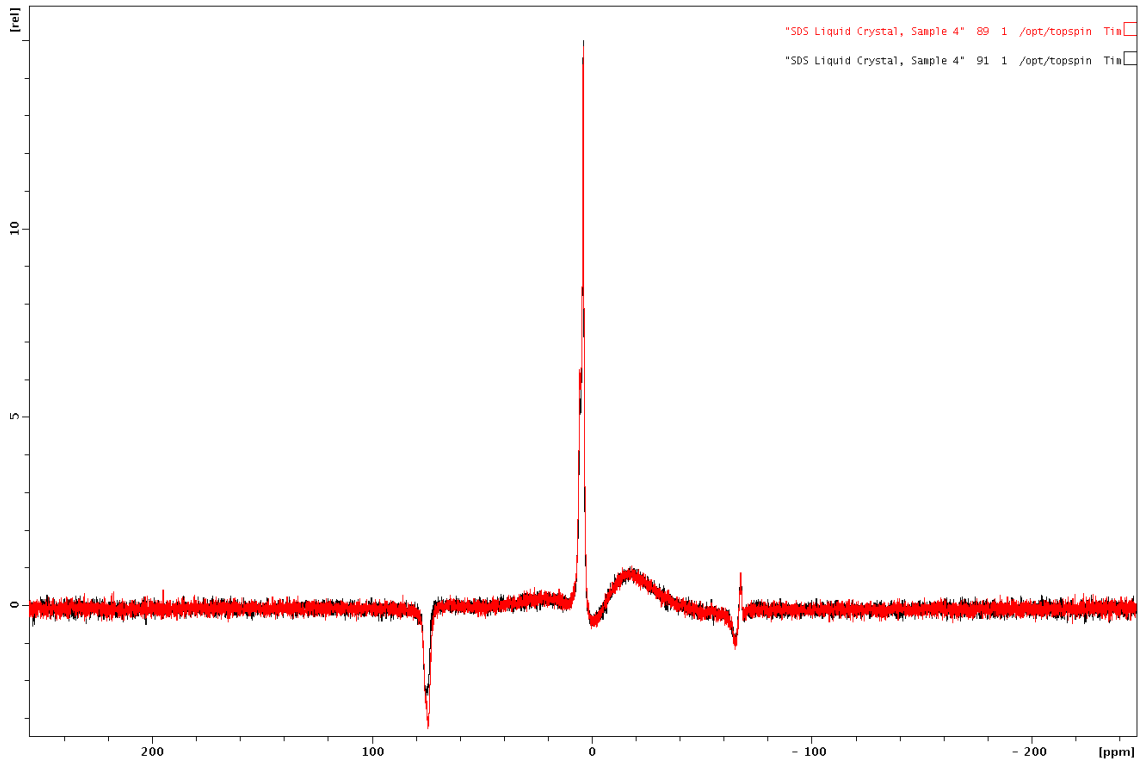


Figure 22: CNOT($|11\rangle$) state (black) and $|10\rangle$ state (red). The application of the CNOT gate produces the expected final state

We find that, when applied to the $|00\rangle$, $|01\rangle$, and $|11\rangle$ states the CNOT gate produces the expected pseudopure state from the truth table – these output spectra are near exact matches of the appropriate pseudopure initial state. However, when the CNOT gate is applied to $|10\rangle$, there is no neat correspondence between the measured and expected output of the CNOT gate (see Fig. 20). While the gate successfully excites the $0 \rightarrow 1$ transition (that is, the left peak) and minimizes the $2 \rightarrow 3$ transition (the right peak), there is a strong excitation of the central transition. As with the residual excitations in our pure state spectra, this may be the result of imperfect phase cycling or imperfect pulse selective. To further investigate the cause of this additional excitation, we may consider the application of two CNOT gates to a given initial pseudopure state.

Two applications of the CNOT gate to a given state should return the initial state, $\text{CNOT}(\text{CNOT}(A)) = A$. Comparisons between the pseudopure states A and $\text{CNOT}(\text{CNOT}(A))$ are given below:

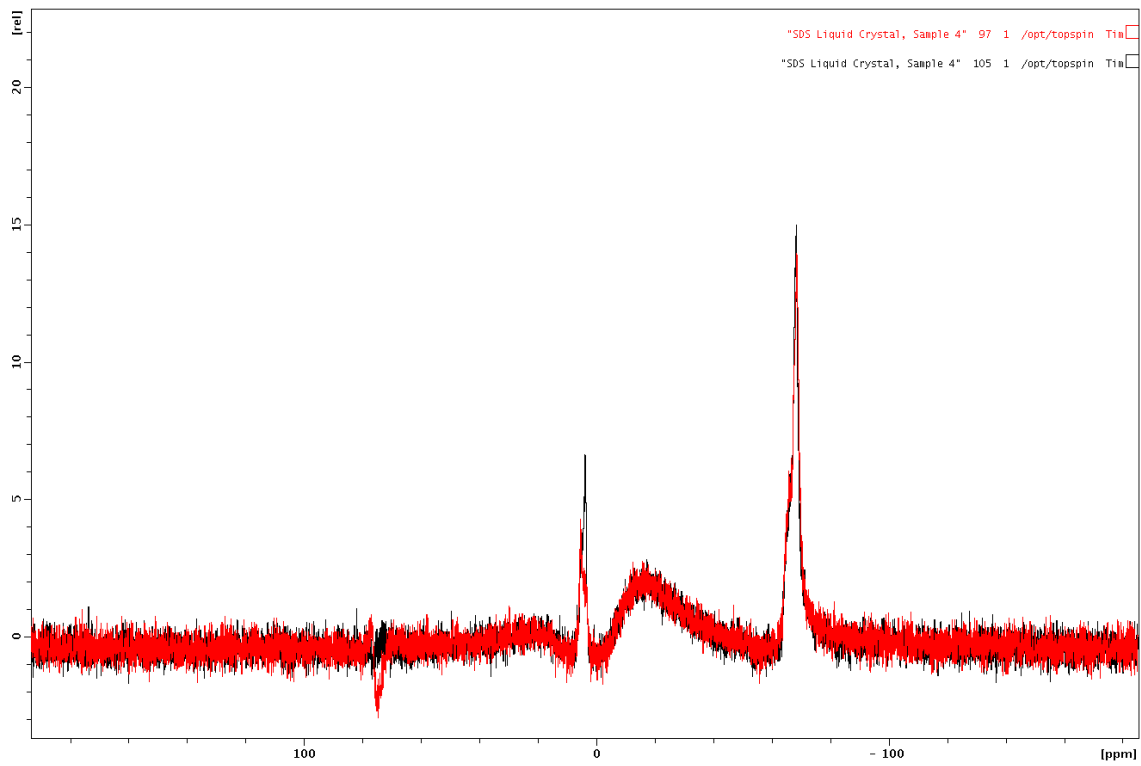


Figure 23: $\text{CNOT}(\text{CNOT}(|00\rangle))$ state (in black) and the $|00\rangle$ initial state (in red). After two applications of the CNOT gate, the left peak has disappeared from the spectrum, and the central peak has increased slightly in amplitude.

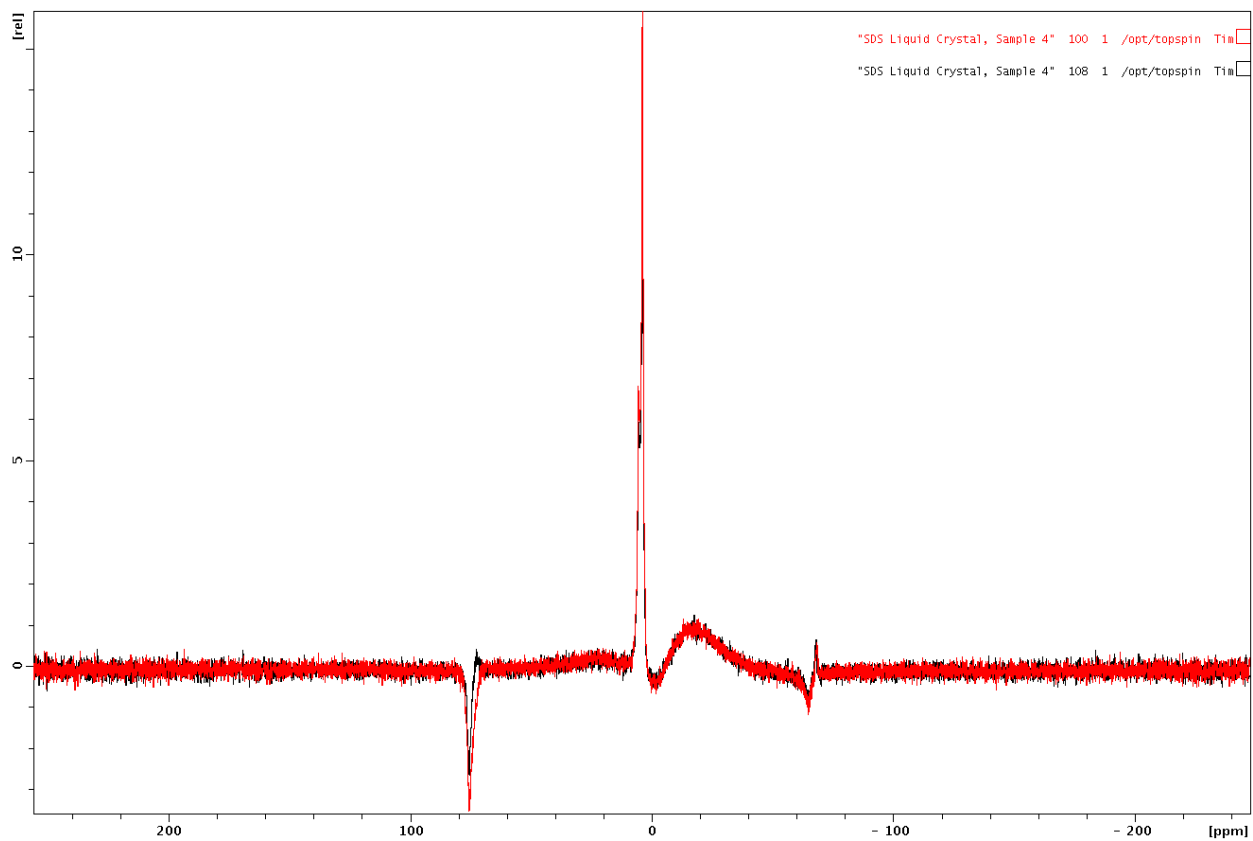


Figure 24: $CNOT(CNOT(|10\rangle))$ state (in black) and the $|10\rangle$ initial state (in red). The application of two CNOT gates to the initial state has decreased the amplitude of both the left and central peaks.

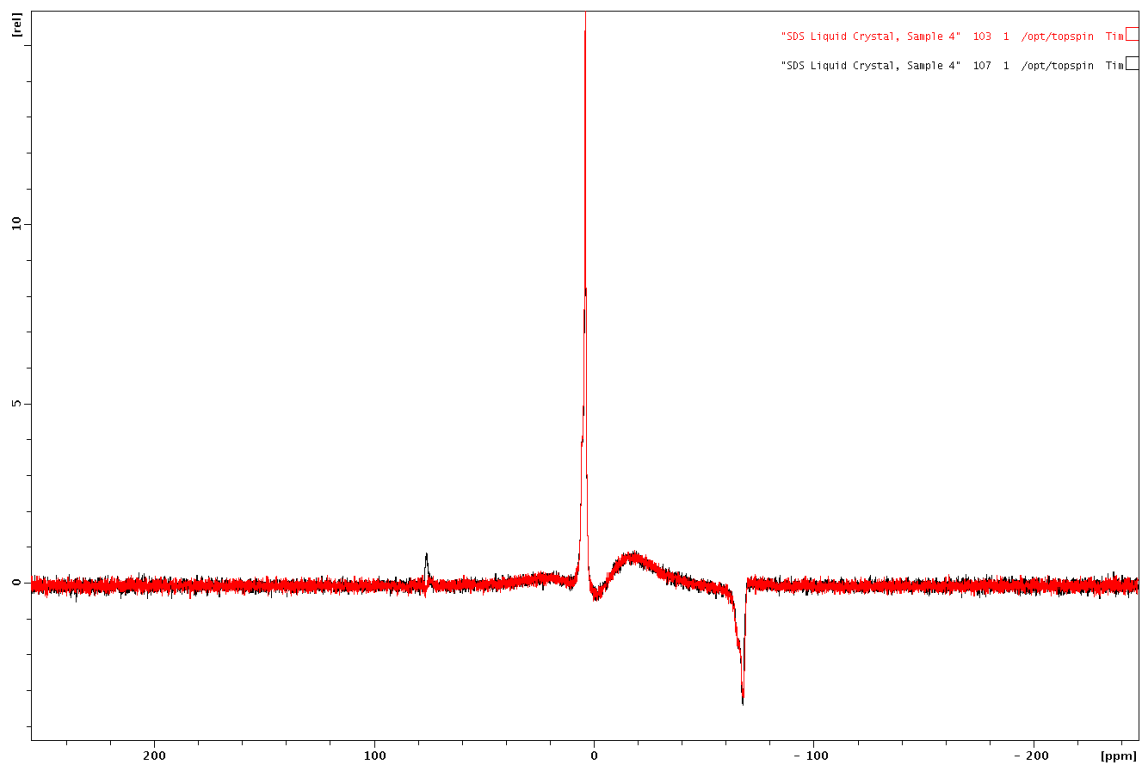


Figure 25: $\text{CNOT}(\text{CNOT}(|01\rangle))$ state (in black) and the $|01\rangle$ initial state (in red). After two applications of the CNOT gate, the amplitude of the left transition goes to zero, while the amplitude of the central transition increases.

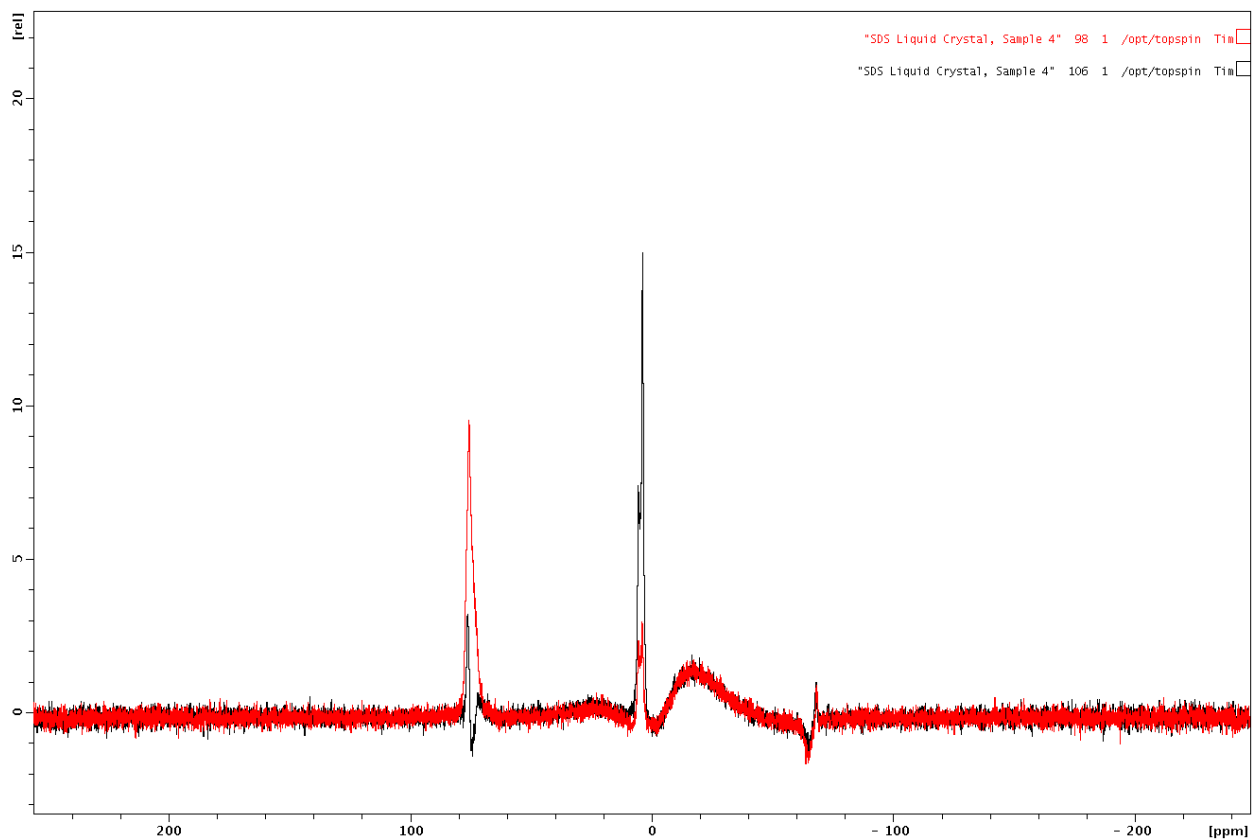


Figure 26: $\text{CNOT}(\text{CNOT}(|11\rangle))$ state (in black) and the $|11\rangle$ initial state (in red). Two applications of the CNOT gate convert the $|11\rangle$ state into the indeterminate state produced by applying the CNOT gate to the $|10\rangle$ state.

For all states except $|11\rangle$, two applications of the CNOT gate returned the system to its initial state. Interestingly, the state produced by $\text{CNOT}(\text{CNOT}(|11\rangle))$ is very similar to the state produced by $\text{CNOT}(|10\rangle)$ (see Fig. 27):

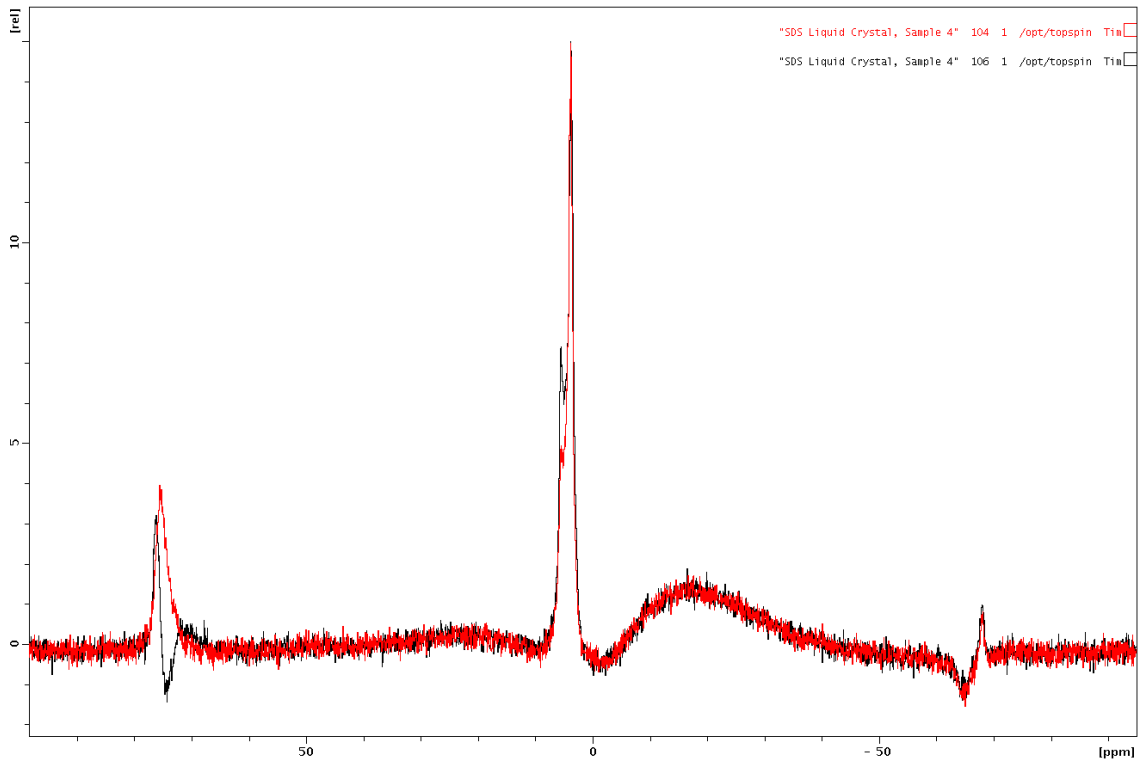


Figure 27: Comparison of the $\text{CNOT}(\text{CNOT}(|11\rangle\rangle)$ (black) and the $\text{CNOT}(|10\rangle\rangle)$ states. Aside from a phase difference in the left peaks, these spectra appear to be largely identical.

While their associated NMR spectra look different, the $\text{CNOT}(|10\rangle\rangle)$ and the $|11\rangle\rangle$ states exhibit the same behavior under the CNOT gate. Applying a CNOT gate to these two states produces the $|10\rangle\rangle$ state, as seen in Figs. 22 and 24. Similarly, two applications of the CNOT gate to $|11\rangle\rangle$ produces the $\text{CNOT}(|10\rangle\rangle)$ state. As seen in Fig. 22, a single application of the CNOT gate to the $|11\rangle\rangle$ state produces the expected $|10\rangle\rangle$ state. However, the second application of the CNOT gate produces the spectrum corresponding to the $\text{CNOT}(|10\rangle\rangle)$ state of Fig. 20 instead of the expected spectra for the $|11\rangle\rangle$ state (see Fig. 27). While the $\text{CNOT}(|10\rangle\rangle)$ and the $|11\rangle\rangle$ spectra look different, they act the same with respect to CNOT gates, leading us to believe that, despite their spectral differences, the two states are closely related. It is possible that these two states have very similar density matrices (explaining their similar behavior under the application of quantum logic gates), but with some small difference in their off-diagonal elements. This small difference could be the result of imperfect phase cycling, as discussed previously. The difference may also be due to some additional liquid crystal phase within the sample. Some

traces of the smetic phase, for instance, would produce the stronger central transition seen in Figs 20 and 26. The presence of this phase would also explain the non-zero central transition observed in the $|00\rangle$ and $|11\rangle$ states. As the central transition is expected in the other two pure states, the influence of the smetic phase would go unnoticed in those states.

5. Conclusions and Future Work

In this work, I have succeeded in reproducing the production of pseudopure initial states and the implementation of quantum logic gates in Na-23 described in the literature [5], [6]. Each of the four pseudopure states was produced using the appropriate pulse sequence. Applying the CNOT gate to each of these states produced the expected final state, with the exception of the $|10\rangle$ state. Applying the CNOT gate to this initial state produced the expected final state, but also excited the central transition. Applying a second CNOT gate to each initial state accurately reproduced each initial state, with the exception of the $|10\rangle$ state. The correspondence between the spectra for $\text{CNOT}(\text{CNOT}(|11\rangle))$ and $\text{CNOT}(|10\rangle)$ seems to indicate some connection between the state produced by applying CNOT to the $|10\rangle$ and the $|11\rangle$ initial state. To further investigate this correspondence, methods of quantum tomography may be used to determine the deviation density matrix elements for each of these two states. In quantum tomography, sequences of selective pulses are applied to a given initial state – these pulses “drag” off-diagonal density matrix elements onto the main diagonal. The diagonal elements are then determined from the amplitudes of an NMR spectra [3], [5]. Since we have already optimized selective pulses for each of these transitions, it should be straightforward to implement this process, allowing us to further explore the peculiarities of the $|10\rangle$ pseudopure state.

While this process – essentially a calibration – has been slow and tedious, its completion represents a large step forward, and allows us to turn our attention toward more interesting problems. Using multiple applications of the CNOT gate discussed here, as well as other quantum logic states, we can implement longer, more complex quantum algorithms on our spin-3/2, two qubit register. Using methods of quantum tomography, we can experimentally determine each elements of the system’s deviation density matrix after these algorithms are applied. The experimentally determined matrix elements can then be compared to the results of SR simulations. Finally, the methods and results described in this project can be generalized to samples with high values of spin. A spin-7/2 nuclei, such as scandium or cesium, in an oriented nematic liquid crystal could act as a three qubit quantum register. This

increased processing power would allow us to implement more complex algorithms, such as a quantum error correction method proposed by Dr. Chi-Kwong Li of William and Mary's Math Department [9].

APPENDIX 1: Pulse Programs to Generate Psuedo-Pure States

A1.1 Pure State $|00\rangle$

```
;pseudo-pure-state-00
;Tim Milbourne, adapted from Bonk, Sinha [3], [6]
;avance-version (3/24/14)
;produces pseudopure state  $|00\rangle$  in spin-3/2 sample

#include <Avance.incl>

1 ze
2 30m
  d1 pl1:f1
  p22:sp1:f1 ph1
  d2
  4u fq=cnst1:f1
  p11:sp1:f1 ph2
  d2
  1u fq = 0:f1
  4u pl2:f1
  p4:f1 ph3
  go=2 ph3
  10m mc #0 to 2 F0(zd)
exit

ph1= 0 0 0 0 2 2 2 2 0 0 0 0 2 2 2 2 0 0 0 0 2 2 2 2 0 0 0 0 2 2 2 2
;ph1= 0 2 0 2 0 2 0 2 0 2 0 2 0 2 0 2 0 2 0 2 0 2 0 2 0 2 0 2 0 2 0 2
;ph2= 0 0 2 2 1 1 3 3 0 0 2 2 1 1 3 3 0 0 2 2 1 1 3 3 0 0 2 2 1 1 3 3
ph2= 0 2 1 3 0 2 1 3 0 2 1 3 0 2 1 3 0 2 1 3 0 2 1 3 0 2 1 3 0 2 1 3
ph3= 0 0 0 0 0 0 0 0 1 1 1 1 1 1 1 1 2 2 2 2 2 2 2 2 3 3 3 3 3 3 3 3

;p11: power level for selective pulse
;p12: power level for non-selective pulse
;p22: 180 degree pulse for central transition
;p11: 90 degree pulse for left transition
;p4: hard, non-selective pulse length
;sp1: pulse shape - use Gaussian of some sort
;cnst1: frequency offset for left transition
;d2: Some tunable delay
;NS :4 * n, total number of scans: NS * TD0

;$Id: t1ir1d,v 1.7 2002/06/12 09:05:15 ber Exp $
```

A1.2 Pure State $|01\rangle$

```
;pseudo-pure-state-01  
;Tim Milbourne, adapted from Bonk, Sinha [3], [6]  
;avance-version (3/24/14)  
;produces pseudopure state  $|00\rangle$  in spin-3/2 sample
```

```
#include <Avance.incl>
```

```
1 ze  
2 30m  
  d1 p1:f1  
  p22:sp1:f1 ph1  
  d2  
  4u fq=cnst1:f1  
  p11:sp1:f1 ph2  
  d2  
  1u fq = 0:f1  
  4u fq=cnst2:f1  
  p32:sp1:f1 ph1  
  d2  
  1u fq = 0:f1  
  4u pl2:f1  
  p4:f1 ph3  
  go=2 ph3  
  10m mc #0 to 2 F0(zd)  
exit
```

```
ph1= 0 0 0 0 2 2 2 2 0 0 0 0 2 2 2 2 0 0 0 0 2 2 2 2 0 0 0 0 2 2 2 2  
ph2= 0 2 1 3 0 2 1 3 0 2 1 3 0 2 1 3 0 2 1 3 0 2 1 3 0 2 1 3 0 2 1 3  
ph3= 0 0 0 0 0 0 0 0 1 1 1 1 1 1 1 1 2 2 2 2 2 2 2 2 3 3 3 3 3 3 3 3
```

```
;p11: power level for selective pulse  
;pl2: power level for non-selective pulse  
;p11: 90 degree pulse for left transition  
;p22: 180 degree pulse for central transition  
;p32: 180 degree pulse for right transition  
;p4: hard, non-selective pulse length  
;sp1: pulse shape - use Gaussian of some sort  
;cnst1: frequency offset for left transition  
;cnst2: frequency offset for right transition  
;d2: Some tunable delay  
;NS :4 * n, total number of scans: NS * TD0
```

```
;$Id: t1ir1d,v 1.7 2002/06/12 09:05:15 ber Exp $
```

A1.3 Pure State $|10\rangle$

```
;pseudo-pure-state-10
;Tim Milbourne, adapted from Bonk, Sinha [3], [6]
;avance-version (3/24/14)
;produces pseudopure state  $|00\rangle$  in spin-3/2 sample
```

```
#include <Avance.incl>
```

```
1 ze
2 30m
  d1 pl1:f1
  p22:sp1:f1 ph1
  d2
  4u fq=cnst1:f1
  p12:sp1:f1 ph1
  d2
  1u fq = 0:f1
  4u fq=cnst2:f1
  p31:sp1:f1 ph2
  d2
  1u fq = 0:f1
  4u pl2:f1
  p4:f1 ph3
  go=2 ph3
  10m mc #0 to 2 F0(zd)
```

```
exit
```

```
ph1= 0 0 0 0 2 2 2 2 0 0 0 0 2 2 2 2 0 0 0 0 2 2 2 2 0 0 0 0 2 2 2 2
;ph1= 0 2 0 2 0 2 0 2 0 2 0 2 0 2 0 2 0 2 0 2 0 2 0 2 0 2 0 2 0 2 0 2
;ph2= 0 0 2 2 1 1 3 3 0 0 2 2 1 1 3 3 0 0 2 2 1 1 3 3 0 0 2 2 1 1 3 3
ph2= 0 2 1 3 0 2 1 3 0 2 1 3 0 2 1 3 0 2 1 3 0 2 1 3 0 2 1 3 0 2 1 3
ph3= 0 0 0 0 0 0 0 0 1 1 1 1 1 1 1 1 2 2 2 2 2 2 2 2 3 3 3 3 3 3 3 3
```

```
;pl1: power level for selective pulse
;p12: power level for non-selective pulse
;p12: 180 degree pulse for left transition
;p22: 180 degree pulse for central transition
;p31: 90 degree pulse for right transition
;p4: hard, non-selective pulse length
;sp1: pulse shape - use Gaussian of some sort
;cnst1: frequency offset for left transition
;cnst2: frequency offset for right transition
;d2: some tunable delay
;NS :4 * n, total number of scans: NS * TD0
```

```
;$Id: t1ir1d,v 1.7 2002/06/12 09:05:15 ber Exp $
```

A1.4 Pure State |11⟩

```
;pseudo-pure-state-11
;Tim Milbourne, adapted from Bonk, Sinha [3], [6]
;avance-version (3/24/14)
;produces pseudopure state |00> in spin-3/2 sample
```

```
#include <Avance.incl>
```

```
1 ze
2 30m
  d1 p1:f1
  p22:sp1:f1 ph1
  d2
  4u fq=cnst2:f1
  p31:sp1:f1 ph2
  d2
  1u fq = 0:f1
  4u pl2:f1
  p4:f1 ph3
  go=2 ph3
  10m mc #0 to 2 F0(zd)
exit
```

```
ph1= 0 0 0 0 2 2 2 2 0 0 0 0 2 2 2 2 0 0 0 0 2 2 2 2 0 0 0 0 2 2 2 2
ph2= 0 2 1 3 0 2 1 3 0 2 1 3 0 2 1 3 0 2 1 3 0 2 1 3 0 2 1 3 0 2 1 3
ph3= 0 0 0 0 0 0 0 0 1 1 1 1 1 1 1 1 2 2 2 2 2 2 2 2 3 3 3 3 3 3 3 3
```

```
;p1: power level for selective pulse
;p2: power level for non-selective pulse
;p22: 180 degree pulse for central transition
;p31: 90 degree pulse for right transition
;p4: hard, non-selective pulse length
;sp1: pulse shape - use Gaussian of some sort
;cnst2: frequency offset for right transition
;d2: Some tunable delay
;NS :4 * n, total number of scans: NS * TD0
```

```
;$Id: tlir1d,v 1.7 2002/06/12 09:05:15 ber Exp $
```

REFERENCES:

- [1] J. Teles, E.R DeAzevedo, J.C.C Freitas, R.S Sarthour, S. Oliveira, & T.J. Bomagamba, *Philosophical Transactions of the Royal Society A*. **370**, (2012), 4770–4793.
- [2] C.P. Slichter, *Principles of Magnetic Resonance*. (1963), 160-174
- [3] F. A. Bonk *et al.*, *Phys. Rev. A*. **69**, 042322 (2004).
- [4] M.H. Levitt, *Spin Dynamics*. (2001), 273-292.
- [5] F. A. Bonk, E. R. de Azevedo, R. S. Sarthour, J. D. Bulnes, J. C. C. Freitas, A. P. Guimaraes, I. S. Oliveira, & T. J. Bonagamba, *Journal of Magnetic Resonance*. **175**, 226 (2005).
- [6] N. Sinha, T. S. Mahesh, K. V. Ramanathan, and A. Kumar, *J. Chem. Phys.* **114**, 4415 (2001).
- [7] S. Chandrasekhar, *Liquid Crystals*. (1992), 1-8.
- [8] G. Burducea, *Romanian Reports in Physics*. **56**, (2004), 87-100.
- [9] Li, C., Nakahara, M., Poon, Y., Sze, N., & Tomita, H. Recovery in quantum error correction for general noise without measurement. eprint arXiv:quant-ph/1102.1618